

Gravitational perturbations of the Kerr geometry: High-accuracy study

Gregory B. Cook* and Maxim Zalutskiy†

Department of Physics, Wake Forest University, Winston-Salem, North Carolina 27109

(Dated: November 20, 2014)

We present results from a new code for computing gravitational perturbations of the Kerr geometry. This new code carefully maintains high precision to allow us to obtain high-accuracy solutions for the gravitational quasinormal modes of the Kerr space-time. Part of this new code is an implementation of a spectral method for solving the angular Teukolsky equation that, to our knowledge, has not been used before for determining quasinormal modes. We focus our attention on two main areas. First, we explore the behavior of these quasinormal modes in the extreme limit of Kerr, where the frequency of certain modes approaches accumulation points on the real axis. We compare our results with recent analytic predictions of the behavior of these modes near the accumulation points and find good agreement. Second, we explore the behavior of solutions of modes that approach the special frequency $M\omega = -2i$ in the Schwarzschild limit. Our high-accuracy methods allow us to more closely approach the Schwarzschild limit than was possible with previous numerical studies. Unlike previous work, we find excellent agreement with analytic predictions of the behavior near this special frequency. We include a detailed description of our methods, and make use of the theory of confluent Heun differential equations throughout. In particular, we make use of confluent Heun polynomials to help shed some light on the controversy of the existence, or not, of quasinormal and total-transmission modes at certain special frequencies in the Schwarzschild limit.

PACS numbers: 04.20.-q, 04.70.Bw, 04.20.Cv, 04.30.Nk

I. INTRODUCTION

Perturbations of the Kerr geometry have received considerable attention. They are important because astrophysical black holes are expected to have some angular momentum J , perhaps even approaching the Kerr limit where $a \equiv J/M \rightarrow M$. Perturbed black holes will ring down to a quiescent state by emitting gravitational waves that may be observed in current or future gravitational wave observatories. Extremal black holes, those where $a \rightarrow M$, are also of interest for quantum field theory. Because of these, and other reasons, perturbations of Kerr continue to receive extensive study.

Of primary interest to this paper are the Quasinormal Modes (QNMs) of the Kerr space-time (see Refs. [1, 2] for excellent reviews of black-hole QNMs). These are the physical modes of a Kerr black hole satisfying the conditions that waves are not allowed to propagate out from the black-hole event horizon or in from infinity. These modes have been explored using various numerical techniques[3–8], and analytically using, for example, WKB methods[9–12] and in the eikonal limit[13, 14]. The standard method for solving these equations numerically is via a continued-fraction technique referred to, in the relativity community, as Leaver’s[5] method. This approach is applied to the coupled radial and angular Teukolsky equations[15] that result from a separation of variables procedure applied to the equations describing linear perturbations of fields propagating in the Kerr geometry. We have implemented an independent, high-

precision version of Leaver’s method for solving the radial equation, but have employed a spectral-type method for solution of the angular equation. Using these tools, we have performed an extensive, high-accuracy survey of the gravitational perturbation modes of Kerr. We have paid particular attention to the Kerr limit for the so-called zero damped modes (ZDMs) and to the Schwarzschild limit ($a \rightarrow 0$) for modes that approach the negative imaginary axis (NIA).

It is well known that, in the Kerr limit, some modes of Kerr approach the real axis[16, 17]. As the complex frequency ω of a mode approaches the real axis, the vanishing of the imaginary part of the frequency implies that the damping time of the mode diverges, hence the label ZDM for these modes. Yang *et al*[18, 19] have recently performed a WKB analysis of these modes. Below we will compare our results with their predictions.

In addition to the QNMs of Kerr, there are also classes of modes known as total transmission modes (TTMs). These correspond to cases where the boundary conditions at the event horizon and at infinity are such as to allow modes to travel only from the left or from the right. Often referred to as *algebraically special* modes because of a particular set of solutions[20], the two cases are distinguished as follows. If perturbations are allowed to flow out at infinity, but only modes flowing *out* of the black hole are allowed at the horizon, then the mode is referred to as TTM-left (TTM_L) since the modes are traveling from the left (assuming a picture where the black hole is to our left and spatial infinity to our right). When these boundary conditions are reversed, the mode is TTM-right (TTM_R) since the modes are traveling from the right. In the context of QNMs these modes are important because there seems to be a correlation with the behavior of the QNMs at the NIA.

* cookgb@wfu.edu

† zalump8@wfu.edu

In the Schwarzschild limit ($a \rightarrow 0$), the TTM frequencies become purely imaginary. These modes also seem to have some correlation to certain overtones of the QNMs. It appears that certain QNMs approach these special frequencies in the Schwarzschild limit; however, it is not possible to use existing numerical techniques to evaluate the mode equations at $a = 0$ in these cases. Thus, there has been some controversy over the existence of QNMs (and the TTMs) at these special frequencies[8, 21, 22]. We have performed high-accuracy surveys in the neighborhood of the NIA to further clarify the behavior of QNMs in this regime.

It is known (see Ref. [23] and references within), but historically somewhat underappreciated in the physics literature, that both the radial and angular Teukolsky equations are examples of the *confluent Heun equation*[24]. In this paper, we will treat the mode equations as confluent Heun equations, making use of techniques for solving these equations when it is useful. In Sec. II, we present the Teukolsky equations and a brief introduction to the confluent Heun equations. We will present enough of the theory of the Heun equations so that readers can follow our discussions. Additional details and references can be found in Ref. [24]. We will next transform each mode equation into an appropriate standard form of the confluent Heun equation. These transformations are not new, and our work closely follows that of Fiziev[23, 25]. For the radial equation, we give a detailed outline of the theory of its solution via Leaver's method. Again, this work is not new (see Refs.[6, 7]) but we present this in the context of the confluent Heun equation for completeness. For the angular mode equation, we implement and test a highly efficient spectral method[26] for finding both the eigenvalues and eigenfunctions.

In Sec. III, we give details of our numerical methods for solving the mode equations and present a small set of our results for comparison with prior solutions. While no novel behavior is seen in any of our solutions, they have been found to unprecedented accuracy. Our solutions have been found using at least 24 decimal digits of precision and our numerical methods have used an absolute tolerance of 10^{-12} conservatively giving us confidence in our results to at least $\pm 10^{-10}$. We compare our highly accurate data sets with the expected behavior[18, 19, 27] for ZDMs, and we reexamine the behavior of QNMs near the algebraically special solution at $M\omega = -2i$. In the latter case, prior numerical work[28] has not found agreement with predicted behavior[22]. However, our high-accuracy results do find good agreement between theory and numerical solutions. Next, we rederive the algebraically special perturbations of Kerr (the TTMs) as examples of finding polynomial solutions of the confluent Heun equation. The fact that some Heun polynomial solutions of the radial equation correspond to the TTMs is not new[29], but we feel it is important to include these examples for completeness. Finally, we make use of these Heun polynomial solutions for the TTMs in the limit that $a = 0$ to reexamine the existence of QNMs and TTM_R

at special frequencies on the NIA.

II. SOLVING THE TEUKOLSKY EQUATIONS

A. The Teukolsky Equations

In terms of Boyer-Lindquist coordinates, the line element of the Kerr metric is given by

$$\begin{aligned} ds^2 = & - \left(1 - \frac{2Mr}{\Sigma} \right) dt^2 \\ & - \frac{4Mra \sin^2 \theta}{\Sigma} dt d\phi + \frac{\Sigma}{\Delta} dr^2 + \Sigma d\theta^2 \\ & + \left(r^2 + a^2 + \frac{2Mra^2 \sin^2 \theta}{\Sigma} \right) \sin^2 \theta d\phi^2, \end{aligned} \quad (1a)$$

$$\Sigma \equiv r^2 + a^2 \cos^2 \theta, \quad (1b)$$

$$\Delta \equiv r^2 - 2Mr + a^2. \quad (1c)$$

Making use of the Newman-Penrose formalism, Teukolsky[15] showed that perturbations of several kinds of fields are governed by a single master equation

$$\begin{aligned} & \left[\frac{(r^2 + a^2)^2}{\Delta} - a^2 \sin^2 \theta \right] \frac{\partial^2 {}_s \psi}{\partial t^2} \\ & + \frac{4Mar}{\Delta} \frac{\partial^2 {}_s \psi}{\partial t \partial \phi} + \left[\frac{a^2}{\Delta} - \frac{1}{\sin^2 \theta} \right] \frac{\partial^2 {}_s \psi}{\partial \phi^2} \\ & - \Delta^{-s} \frac{\partial}{\partial r} \left(\Delta^{s+1} \frac{\partial_s \psi}{\partial r} \right) - \frac{1}{\sin \theta} \frac{\partial}{\partial \theta} \left(\sin \theta \frac{\partial_s \psi}{\partial \theta} \right) \\ & - 2s \left[\frac{a(r - M)}{\Delta} + \frac{i \cos \theta}{\sin^2 \theta} \right] \frac{\partial_s \psi}{\partial \phi} \\ & - 2s \left[\frac{M(r^2 - a^2)}{\Delta} - r - ia \cos \theta \right] \frac{\partial_s \psi}{\partial t} \\ & + (s^2 \cot^2 \theta - s) {}_s \psi = 4\pi \Sigma T, \end{aligned} \quad (2)$$

where T represents source terms and ${}_s \psi$ is a scalar of spin weight s . Scalar fields are represented by $s = 0$, spin- $\frac{1}{2}$ fields by $s = \pm \frac{1}{2}$, electromagnetic fields by $s = \pm 1$, and gravitational perturbations by $s = \pm 2$. Assuming the vacuum case ($T = 0$), Eq. (2) separates if we let

$${}_s \psi(t, r, \theta, \phi) = e^{-i\omega t} e^{im\phi} S(\theta) R(r). \quad (3)$$

With $x \equiv \cos \theta$, the function $S(\theta) = {}_s S_{\ell m}(x; a\omega)$ is the spin-weighted spheroidal function satisfying

$$\begin{aligned} & \partial_x \left[(1 - x^2) \partial_x [{}_s S_{\ell m}(x; c)] \right] \\ & + \left[(cx)^2 - 2csx + s + {}_s A_{\ell m}(c) \right. \\ & \left. - \frac{(m + sx)^2}{1 - x^2} \right] {}_s S_{\ell m}(x; c) = 0, \end{aligned} \quad (4)$$

where c ($= a\omega$) is the oblateness parameter, m the azimuthal separation constant, and ${}_s A_{\ell m}(c)$ is the angular

separation constant. The radial function $R(r)$ must satisfy

$$\Delta^{-s} \frac{d}{dr} \left[\Delta^{s+1} \frac{dR(r)}{dr} \right] + \left[\frac{K^2 - 2is(r-M)K}{\Delta} + 4is\omega r - \lambda \right] R(r) = 0, \quad (5a)$$

where

$$K \equiv (r^2 + a^2)\omega - am, \quad (5b)$$

$$\lambda \equiv {}_s A_{\ell m}(a\omega) + a^2\omega^2 - 2am\omega. \quad (5c)$$

Equations (4) and (5a) are coupled. Given a value for ${}_s A_{\ell m}(a\omega)$, Eq. (5a) is solved for the complex frequency ω . Given a complex frequency ω , Eq. (4) is an eigenvalue problem for ${}_s A_{\ell m}(a\omega)$. In both cases, appropriate boundary conditions must be supplied.

B. The confluent Heun equation

A Heun equation is a second-order linear differential equation with four regular singular points. The *confluent Heun equation* occurs when one regular singular point is lost by confluence with another and the point at infinity becomes irregular. Both Eqs. (4) and (5a) are examples of the confluent Heun equation. Reference [24] contains a very useful summary of the various forms of Heun's differential equations and their solutions, and this section represents a summary of the important points relevant to this paper.

A useful form of the confluent Heun equation is the so-called *nonsymmetrical canonical form*:

$$\frac{d^2 H(z)}{dz^2} + \left(4p + \frac{\gamma}{z} + \frac{\delta}{z-1} \right) \frac{dH(z)}{dz} + \frac{4\alpha pz - \sigma}{z(z-1)} H(z) = 0. \quad (6)$$

Much of the theory of solutions to the confluent Heun equation is based on this form of the equation. It is defined by five parameters: p , α , γ , δ , and σ . It has a regular singular point at $z = 0$ with characteristic exponents $\{0, 1 - \gamma\}$ so solutions in general behave like

$$\lim_{z \rightarrow 0} H(z) \sim 1 \quad \text{or} \quad z^{1-\gamma}. \quad (7)$$

There is a regular singular point at $z = 1$ with characteristic exponents $\{0, 1 - \delta\}$ so solutions in general behave like

$$\lim_{z \rightarrow 1} H(z) \sim 1 \quad \text{or} \quad (z-1)^{1-\delta}. \quad (8)$$

And there is an irregular singular point at $z = \infty$ where solutions in general behave like

$$\lim_{z \rightarrow \infty} H(z) \sim z^{-\alpha} \quad \text{or} \quad e^{-4pz} z^{\alpha-\gamma-\delta}. \quad (9)$$

Other forms of the confluent Heun equation are common. If we let $z \rightarrow 1 - 2z$ and define

$$H^{(B)}(z) \equiv (z-1)^{\frac{\mu+\nu}{2}} (z+1)^{\frac{\mu-\nu}{2}} e^{-pz} H((1-z)/2), \quad (10)$$

we obtain the *Bôcher symmetrical form*:

$$\begin{aligned} & \frac{d}{dz} \left((z^2 - 1) \frac{dH^{(B)}(z)}{dz} \right) \\ & + \left(-p^2(z^2 - 1) + 2p\beta z - \lambda \right. \\ & \left. - \frac{\mu^2 + \nu^2 + 2\mu\nu z}{z^2 - 1} \right) H^{(B)}(z) = 0, \end{aligned} \quad (11)$$

where the new parameters β , λ , μ , and ν are defined by

$$\begin{aligned} \gamma &= \mu + \nu + 1, & \delta &= \mu - \nu + 1, & \alpha &= -\beta + \mu + 1, \\ \sigma &= \lambda - 2p(\beta - \mu - \nu - 1) - \mu(\mu + 1), \end{aligned} \quad (12)$$

and the regular singular points are now at $z = \pm 1$. Equation (11) is also referred to as the *generalized spheroidal equation*. Finally, the *normal symmetrical form*, or the *normal form of the generalized spheroidal equation*, is obtained by the transformation

$$H^{(B)}(z) \equiv (1 - z^2)^{-\frac{1}{2}} H^{(N)}(z) \quad (13)$$

and takes the form

$$\begin{aligned} & (z^2 - 1) \frac{d^2 H^{(N)}(z)}{dz^2} \\ & + \left(-p^2(z^2 - 1) + 2p\beta z - \lambda \right. \\ & \left. - \frac{\mu^2 + \nu^2 - 1 + 2\mu\nu z}{z^2 - 1} \right) H^{(N)}(z) = 0. \end{aligned} \quad (14)$$

1. Local solutions

Power series solutions local to each of the singular points can be defined in terms of two functions: $Hc^{(a)}(p, \alpha, \gamma, \delta, \sigma; z)$ and $Hc^{(r)}(p, \alpha, \gamma, \delta, \sigma; z)$. These are defined by

$$Hc^{(a)}(p, \alpha, \gamma, \delta, \sigma; 0) = 1, \quad (15a)$$

$$Hc^{(a)}(p, \alpha, \gamma, \delta, \sigma; z) = \sum_{k=0}^{\infty} c_k^{(a)} z^k, \quad (15b)$$

and

$$\lim_{z \rightarrow \infty} z^\alpha Hc^{(r)}(p, \alpha, \gamma, \delta, \sigma; z) = 1, \quad (16a)$$

$$Hc^{(r)}(p, \alpha, \gamma, \delta, \sigma; z) = \sum_{k=0}^{\infty} c_k^{(r)} z^{-\alpha-k}. \quad (16b)$$

The coefficients $c_k^{(a)}$ and $c_k^{(r)}$ are defined by three-term recurrence relations

$$0 = f_k^{(a)} c_{k+1}^{(a)} + g_k^{(a)} c_k^{(a)} + h_k^{(a)} c_{k-1}^{(a)}, \quad (17a)$$

$$\text{with } c_{-1}^{(a)} = 0, \quad c_0^{(a)} = 1,$$

$$g_k^{(a)} = k(k - 4p + \gamma + \delta - 1) - \sigma, \quad (17b)$$

$$f_k^{(a)} = -(k+1)(k+\gamma), \quad (17c)$$

$$h_k^{(a)} = 4p(k+\alpha-1), \quad (17d)$$

and

$$0 = f_k^{(r)} c_{k+1}^{(r)} + g_k^{(r)} c_k^{(r)} + h_k^{(r)} c_{k-1}^{(r)}, \quad (18a)$$

$$\text{with } c_{-1}^{(r)} = 0, \quad c_0^{(r)} = 1,$$

$$g_k^{(r)} = (k+\alpha)(k+4p+\alpha-\gamma-\delta+1) - \sigma, \quad (18b)$$

$$f_k^{(r)} = -4p(k+1), \quad (18c)$$

$$h_k^{(r)} = -(k+\alpha-1)(k+\alpha-\gamma). \quad (18d)$$

The solutions local to the regular singular points can be written in terms of $Hc^{(a)}$. The two solutions local to $z=0$ are given by

$$Hc^{(a)}(p, \alpha, \gamma, \delta, \sigma; z), \quad (19a)$$

$$z^{1-\gamma} Hc^{(a)}(p, \alpha+1-\gamma, 2-\gamma, \delta, \quad (19b)$$

$$\sigma + (1-\gamma)(4p-\delta); z).$$

Local to $z=1$ we have

$$Hc^{(a)}(-p, \alpha, \delta, \gamma, \sigma - 4p\alpha; 1-z) \quad (19c)$$

$$(z-1)^{1-\delta} Hc^{(a)}(-p, \alpha+1-\delta, 2-\delta, \gamma, \quad (19d)$$

$$\sigma - (1-\delta)\gamma - 4p(\alpha+1-\delta); 1-z).$$

The two solutions local to the irregular singular point at $z=\infty$ are

$$Hc^{(r)}(p, \alpha, \gamma, \delta, \sigma; z) \quad (19e)$$

$$e^{-4pz} Hc^{(r)}(-p, -\alpha + \gamma + \delta, \gamma, \delta, \sigma - 4p\gamma; z). \quad (19f)$$

2. Confluent Heun functions

The term *confluent Heun function* is used for solutions that are simultaneously Frobenius solutions for two adjacent singular points. Such functions naturally arise in the solution of eigenvalue problems. In this case, boundary conditions are imposed at the two singular points, and the value of a particular parameter in the equation is found that allows both boundary conditions to be satisfied. The solutions we seek for the angular and radial Teukolsky equations, Eqs. (4) and (5a) fall into this category. There are many ways of finding these solutions and we will address this further below.

3. Polynomial solutions

An important subset of the confluent Heun functions are the *confluent Heun polynomials*. These solutions are simultaneously Frobenius solutions of all three singular points. This requires that the series solutions terminate yielding polynomial solutions. A necessary, but not sufficient condition for this to occur is for the second parameter, α , of either Eq. (15) or (16) to be a nonpositive integer $-q$. In this case, we find from either Eq. (17d) or (18d) that $h_{q+1}^{(a,r)} = 0$. If $c_{q+1}^{(a,r)} = 0$ also holds, then the infinite series will terminate, yielding a polynomial solution. This second condition, referred to as a $\Delta_{q+1} = 0$ condition, is satisfied by the vanishing of the determinant

$$\begin{vmatrix} g_0 & f_0 & 0 & \cdots & 0 \\ h_1 & g_1 & f_1 & \ddots & 0 \\ 0 & h_2 & g_2 & \ddots & 0 \\ 0 & 0 & \ddots & \ddots & \ddots \\ 0 & 0 & \cdots & h_q & g_q \end{vmatrix}. \quad (20)$$

Noting the form of the $g_k^{(a,r)}$ coefficients in Eqs. (17b) and (18b), we see that the $\Delta_{q+1} = 0$ condition can be viewed as an eigenvalue problem for the allowed values of σ . The $q+1$ eigenvalues are labeled σ_{nq} , and can be ordered such that $\sigma_{0q} < \sigma_{1q} < \cdots < \sigma_{qq}$. So, given a local solution defined by $Hc^{(a,r)}(p, -q, \gamma, \delta, \sigma; z)$, a polynomial solution $Hc_{nq}(p, \gamma, \delta; z)$ exists if $\sigma_{nq} = \sigma$.

C. The radial Teukolsky equation

The radial Teukolsky equation, Eq. (5a), has regular singular points at the inner and outer horizons. These are located at the roots, r_\pm , of $\Delta = 0$:

$$r_\pm = M \pm \sqrt{M^2 - a^2}. \quad (21)$$

The outer or event horizon is labeled by r_+ and the inner or Cauchy horizon by r_- . $r = \infty$ is an irregular singular point. We can rewrite Eq. (5a) in nonsymmetrical canonical form by making the following transformation[25]:

$$R(r) = (r - r_+)^{\xi} (r - r_-)^{\eta} e^{\zeta r} H(r), \quad (22)$$

where the parameters ζ , ξ , and η must be fixed to be

$$\zeta = \pm i\omega \equiv \zeta_\pm, \quad (23a)$$

$$\xi = \frac{-s \pm (s + 2i\sigma_+)}{2} \equiv \xi_\pm, \quad (23b)$$

$$\eta = \frac{-s \pm (s - 2i\sigma_-)}{2} \equiv \eta_\pm, \quad (23c)$$

where

$$\sigma_\pm \equiv \frac{2\omega Mr_\pm - ma}{r_+ - r_-}. \quad (24)$$

Before proceeding further, we define the following dimensionless variables:

$$\bar{r} \equiv \frac{r}{M}, \quad (25a)$$

$$\bar{a} \equiv \frac{a}{M}, \quad (25b)$$

$$\bar{\omega} \equiv M\omega, \quad (25c)$$

$$\bar{\zeta} \equiv M\zeta, \quad (25d)$$

It is also useful to transform the radial coordinate. There are many useful ways to do this[25], but here we will focus on

$$z \equiv \frac{r - r_-}{r_+ - r_-} = \frac{\bar{r} - \bar{r}_-}{\bar{r}_+ - \bar{r}_-}. \quad (26)$$

All eight possible combinations of the parameters in Eq. (23) reduce Eq. (5a) to the form of Eq. (6) when we define

$$p = (\bar{r}_+ - \bar{r}_-) \frac{\bar{\zeta}}{2} \quad (27a)$$

$$\alpha = 1 + s + \xi + \eta - 2\bar{\zeta} + s \frac{i\bar{\omega}}{\bar{\zeta}} \quad (27b)$$

$$\gamma = 1 + s + 2\eta \quad (27c)$$

$$\delta = 1 + s + 2\xi \quad (27d)$$

$$\sigma = {}_s A_{\ell m}(\bar{a}\bar{\omega}) + \bar{a}^2 \bar{\omega}^2 - 8\bar{\omega}^2 + p(2\alpha + \gamma - \delta) \quad (27e)$$

$$+ \left(1 + s - \frac{\gamma + \delta}{2}\right) \left(s + \frac{\gamma + \delta}{2}\right).$$

Each of these eight forms produce the same pair of local solutions at each singular point. With $R(z) \sim z^\eta (z-1)^\xi e^{(\bar{r}_+ - \bar{r}_-)\bar{\zeta}z} H(z)$, we find

$$\lim_{z \rightarrow 0} R(z) \sim z^{-s+i\sigma_-} \quad \text{or} \quad z^{-i\sigma_-}, \quad (28a)$$

$$\lim_{z \rightarrow 1} R(z) \sim (z-1)^{-s-i\sigma_+} \quad \text{or} \quad (z-1)^{i\sigma_+}, \quad (28b)$$

$$\lim_{z \rightarrow \infty} R(z) \sim z^{-1-2s+2i\bar{\omega}} e^{i(\bar{r}_+ - \bar{r}_-)\bar{\omega}z} \quad (28c)$$

$$\text{or} \quad z^{-1-2i\bar{\omega}} e^{-i(\bar{r}_+ - \bar{r}_-)\bar{\omega}z}.$$

Given the sign choice made on ω in Eq. (3), we see that the first form of Eq. (28b) corresponds to waves propagating into the black-hole event horizon, and the first form of Eq. (28c) corresponds to waves propagating out at infinity, the appropriate boundary conditions for QNMs (see the Appendix for details). Each of the eight possible choices for the parameters $\{\zeta, \xi, \eta\}$ corresponds to assigning each of the pairs of physical solutions in Eq. (28) to a corresponding pair from Eq. (19). In particular, ξ fixes the correspondence at the event horizon. The choice of $\xi = \xi_-$ means that Eq. (19c) corresponds to the case of waves propagating into the black hole, and Eq. (19d) corresponds to waves propagating out of the black hole. The choice of ζ fixes the correspondence at infinity. The choice $\zeta = \zeta_+$ means that Eq. (19e) corresponds to the case of waves propagating out at infinity, and Eq. (19f) corresponds to waves propagating in

from infinity. The choice of η fixes the correspondence at the Cauchy horizon. These mappings become particularly important when exploring the polynomial solutions of the radial equation below.

1. Confluent Heun functions

In this paper, our main goal in solving the radial Teukolsky equation is to determine the QNMs of Kerr. These solutions will not, in general, correspond to polynomial solutions, but will be confluent Heun functions. For QNMs, we want the boundary condition at the horizon to allow waves to propagate into the black hole, and waves to propagate out at infinity. If we choose $\xi = \xi_-$, then the characteristic exponent at $z = 1$ is zero, so Eq. (19c) represents the desired boundary condition. With the choice $\zeta = \zeta_+$, Eq. (19e) represents the desired boundary condition at $z = \infty$. From Eq. (16a) we see that $\lim_{z \rightarrow \infty} H(z) = z^{-\alpha}$. If we choose

$$H(z) = z^{-\alpha} \bar{R}(z), \quad (29)$$

then we guarantee that $\bar{R}(z)$ tends to a finite number at both boundaries.

The confluent Heun function we seek will be simultaneously a Frobenius solution for both $z = 1$ and $z = \infty$. The radius of convergence for the local solutions is in general the distance to the next singular point. Thus, the series solution around $z = 1$ has a radius of convergence no larger than 1, far short of infinity. We closely follow Leaver's approach[5, 6] to circumvent this problem.

Let $z \rightarrow \frac{z-1}{z}$ so that the regular singular point at \bar{r}_- is now pushed to $z = -\infty$. The regular singular point at \bar{r}_+ is now located at $z = 0$, and the irregular singular point at infinity is now located at $z = 1$. The differential equation now becomes

$$z(1-z)^2 \frac{d^2 \hat{R}(z)}{dz^2} + [D_0 + D_1 z + D_2 z^2] \frac{d\hat{R}(z)}{dz} + [D_3 + D_4 z] \hat{R}(z) = 0, \quad (30)$$

with $\bar{R}(z) = \hat{R}((z-1)/z)$ and

$$D_0 = \delta = 1 + s + 2\xi, \quad (31a)$$

$$D_1 = 4p - 2\alpha + \gamma - \delta - 2, \quad (31b)$$

$$D_2 = 2\alpha - \gamma + 2, \quad (31c)$$

$$D_3 = \alpha(4p - \delta) - \sigma, \quad (31d)$$

$$D_4 = \alpha(\alpha - \gamma + 1). \quad (31e)$$

Expanding $\hat{R}(z)$ in Eq. (30) in terms of the Taylor series $\hat{R}(z) = \sum_{n=0}^{\infty} a_n z^n$, we obtain the three-term recurrence relation where the coefficients, a_n , satisfy

$$0 = a_0 \beta_0 + a_1 \alpha_0, \quad (32a)$$

$$0 = a_{n+1} \alpha_n + a_n \beta_n + a_{n-1} \gamma_n, \quad (32b)$$

with

$$\alpha_n \equiv n^2 + (D_0 + 1)n + D_0, \quad (32c)$$

$$\beta_n \equiv -2n^2 + (D_1 + 2)n + D_3, \quad (32d)$$

$$\gamma_n \equiv n^2 + (D_2 - 3)n + D_4 - D_2 + 2. \quad (32e)$$

With $a_0 = 1$, we are guaranteed to obey the boundary condition at the event horizon ($z = 0$), but must find the solution that yields a finite answer at infinity ($z = 1$). A three-term recurrence relation such as Eq. (32b) will have two linearly independent solutions. To understand their behaviors, consider the radius of convergence $\rho_a \equiv \lim_{n \rightarrow \infty} \frac{a_{n+1}}{a_n}$. From Eq. (32b) we find

$$\lim_{n \rightarrow \infty} \left\{ \frac{a_{n+1}}{a_n} + \frac{\beta_n}{\alpha_n} + \frac{a_{n-1}}{a_n} \frac{\gamma_n}{\alpha_n} \right\} = \rho_a - 2 + \frac{1}{\rho_a} = 0, \quad (33)$$

which has the double root $\rho_a = 1$. Since we do not have distinct roots, we must consider higher-order behavior in $\lim_{n \rightarrow \infty} \frac{a_{n+1}}{a_n}$. We assume

$$\boxed{\lim_{n \rightarrow \infty} \frac{a_{n+1}}{a_n} = 1 + \frac{u_1}{\sqrt{n}} + \frac{u_2}{n} + \frac{u_3}{n^{\frac{3}{2}}} + \dots} \quad (34)$$

If we consider

$$\begin{aligned} \left(\lim_{n \rightarrow \infty} \frac{\frac{d}{dn} a_{n+1}}{a_n} \right) &\approx \lim_{n \rightarrow \infty} \left(\frac{a_{n+1} - a_n}{a_n} \right) \\ &= \frac{u_1}{\sqrt{n}} + \frac{u_2}{n} + \frac{u_3}{n^{\frac{3}{2}}} + \dots, \end{aligned} \quad (35)$$

then

$$\lim_{n \rightarrow \infty} \ln(a_n) \approx \int \left(\frac{u_1}{\sqrt{n}} + \frac{u_2}{n} + \frac{u_3}{n^{\frac{3}{2}}} + \dots \right) dn. \quad (36)$$

The result is

$$\lim_{n \rightarrow \infty} a_n \propto n^{u_2} e^{2u_1 \sqrt{n}}. \quad (37)$$

Inserting Eq. (34) into Eq. (33), we find

$$u_1 = \pm \sqrt{-4p}, \quad (38a)$$

$$u_2 = -\frac{1}{4}(8p - 4\alpha + 2\gamma + 2\delta + 3), \quad (38b)$$

$$\begin{aligned} u_3 = \frac{1}{32u_1} [32p(2p - 4\alpha + \gamma + 3\delta + 4) \\ + 4(\gamma + \delta)(\gamma + \delta - 2) + 16\sigma + 3], \end{aligned} \quad (38c)$$

The asymptotic behavior of a_n is dominated by the exponential term in Eq. (37), and the two solutions for u_1 correspond to the two possible asymptotic behaviors for a_n . The solution where $\text{Re}(u_1) < 0$ we define as $a_n \equiv f_n$, the other solution is labeled g_n . Since these two solutions have the property $\lim_{n \rightarrow \infty} \frac{f_n}{g_n} = 0$, when it exists, f_n will be the *minimal solution* of Eq. (32b) while g_n will

be a dominant solution. With $\bar{\zeta} = \bar{\zeta}_+ = i\bar{\omega}$, so long as $\text{Im}(\bar{\omega}) < 0$, $\text{Re}(\sqrt{-4p}) < 0$ and $u_1 = +\sqrt{-4p}$ is associated with the minimal solution and $u_1 = -\sqrt{-4p}$ with a dominant solution.

Defining the ratio $r_n \equiv \frac{a_{n+1}}{a_n}$, Eq. (32b) can be written as

$$\frac{a_{n+1}}{a_n} \equiv r_n = \frac{-\gamma_{n+1}}{\beta_{n+1} + \alpha_{n+1}r_{n+1}} \quad n = 0, 1, 2, \dots, \quad (39)$$

which is a recursive form equivalent to the continued fraction

$$r_n = \frac{-\gamma_{n+1}}{\beta_{n+1} -} \frac{\alpha_{n+1}\gamma_{n+2}}{\beta_{n+2} -} \frac{\alpha_{n+2}\gamma_{n+3}}{\beta_{n+3} -} \dots \quad (40)$$

The usefulness of this continued fraction comes from a theorem due to Pincherle (see Ref. [30]).

Theorem 1 (Pincherle) *The continued fraction r_0 converges if and only if the recurrence relation Eq. (32b) possesses a minimal solution $a_n = f_n$, with $f_0 \neq 0$. In case of convergence, moreover, one has $\frac{f_{n+1}}{f_n} = r_n$ with $n = 0, 1, 2, \dots$ provided $f_n \neq 0$.*

Because the recurrence terminates, we have the special condition given by Eq. (32a). This tells us that

$$r_0 = \frac{f_1}{f_0} = -\frac{\beta_0}{\alpha_0}. \quad (41)$$

Therefore, the continued fraction r_0 does converge, and by Theorem 1, the coefficients $a_n = f_n$ are the minimal solution of Eq. (32b). Moreover, the continued fraction cannot converge to any arbitrary value, but must converge to the value of Eq. (41). This will only be possible when $\bar{\omega}$ takes on certain values, the QNMs.

Combining Eqs. (39) and (41), we obtain a general continued fraction equation

$$0 = \beta_0 - \frac{\alpha_0\gamma_1}{\beta_1 -} \frac{\alpha_1\gamma_2}{\beta_2 -} \frac{\alpha_2\gamma_3}{\beta_3 -} \dots, \quad (42)$$

that is considered a function of $\bar{\omega}$. For fixed s , m , and \bar{a} , and for a given value of ${}_sA_{\ell m}(\bar{a}\bar{\omega})$, we can solve for the eigenvalues $\bar{\omega}$ of Eq. (30) by finding the roots of Eq. (42). This approach for solving the radial Teukolsky equation is referred to in the literature as *Leaver's method*.

In practice, the continued fraction must be truncated by some means. We define a truncated version of this continued fraction as

$$\text{Cf}(N) \equiv \beta_0 - \frac{\alpha_0\gamma_1}{\beta_1 -} \frac{\alpha_1\gamma_2}{\beta_2 -} \frac{\alpha_2\gamma_3}{\beta_3 -} \dots \frac{\alpha_{N-1}\gamma_N}{\beta_N + \alpha_N r_N}. \quad (43)$$

It is also useful to define the n th inversion of this truncated continued fraction:

$$\begin{aligned} \text{Cf}(n; N) \equiv &\beta_n - \frac{\alpha_{n-1}\gamma_n}{\beta_{n-1} -} \frac{\alpha_{n-2}\gamma_{n-1}}{\beta_{n-2} -} \dots \frac{\alpha_0\gamma_1}{\beta_0} \\ &- \frac{\alpha_n\gamma_{n+1}}{\beta_{n+1} -} \frac{\alpha_{n+1}\gamma_{n+2}}{\beta_{n+2} -} \dots \frac{\alpha_{N-1}\gamma_N}{\beta_N + \alpha_N r_N}, \end{aligned} \quad (44)$$

with $\text{Cf}(0; N) \equiv \text{Cf}(N)$ and $0 \leq n < N$.

In order to find roots of $\text{Cf}(n; N)$, the truncated continued fraction must be explicitly evaluated for some appropriate value of N . Using Lentz's method[31], N is determined dynamically by demanding that the change in $\text{Cf}(n; N)$ caused by adding additional terms is below some tolerance. This is a “top-down” approach, evaluating the continued fraction as a ratio of two infinite series. With this method, a value for r_N is never needed. An alternate method is to choose a value for N , assume $r_N = 0$, and evaluate $\text{Cf}(n; N)$ from the “bottom up”. This method is less prone to rounding errors, but one must test various values of N to ensure that the desired tolerance in $\text{Cf}(n; N)$ has been reached. An even better approach, first used in the context of QNMs by Nollert[7], is to use Eq. (34) with $n \mapsto N$ to approximate r_N . We use this approach to solve the radial Teukolsky equation, and use terms out through u_5 in our approximation of r_N .

D. The angular Teukolsky equation

The angular Teukolsky equation, Eq. (4), has regular singular points at $x = \pm 1$ and an irregular singular point at infinity. It is an example of the confluent Heun equation in Bôcher symmetrical form with

$$p = c, \quad (45a)$$

$$\beta = s, \quad (45b)$$

$$\lambda = {}_s A_{\ell m}(c) + s(s+1), \quad (45c)$$

and any of the 8 possible combinations of

$$\mu = \pm m \quad \text{and} \quad \nu = \pm s \quad (45d)$$

or

$$\mu = \pm s \quad \text{and} \quad \nu = \pm m. \quad (45e)$$

Using exactly the same methods discussed in Sec. II C, Leaver's method can be used to solve a continued fraction equation derived from Eq. (4) for its eigenvalues ${}_s A_{\ell m}(c)$. Following Leaver[5], it is common to expand ${}_s S_{\ell m}(x; c)$ as

$${}_s S_{\ell m}(x; c) = \sum_{n=0}^{\infty} b_n (1+x)^n. \quad (46)$$

Other approaches are possible[32], and several others have used an expansion in terms of Jacobi polynomials[6, 33] instead of powers of $1+x$. The latter approach also leads to a continued fraction equation, the roots of which yield the eigenvalues associated with a minimal solution of Eq. (4). However, we have chosen to solve the angular Teukolsky equation using a direct spectral eigenvalue approach[26]. This method does not seem to have been used previously in the computation of QNMs and

we developed this method independently, only learning of its prior use by Hughes[26] after submission of this manuscript. His derivation is slightly different than ours, and contains a few errors. We present a full derivation below.

1. The spectral eigenvalue method

The spin-weighted spheroidal harmonics ${}_s S_{\ell m}(\theta, \phi; c)$ are generalizations of the spin-weighted spherical harmonics ${}_s Y_{\ell m}(\theta, \phi) = {}_s S_{\ell m}(\theta, \phi; 0)$, where s is the spin weight of the harmonic and c is the oblateness parameter. The angular dependence separates as

$${}_s S_{\ell m}(\theta, \phi; c) \equiv \frac{1}{2\pi} {}_s S_{\ell m}(\cos \theta; c) e^{im\phi}. \quad (47)$$

The spin-weighted spheroidal function ${}_s S_{\ell m}(x; c)$ satisfies the angular Teukolsky equation (4). These functions are direct generalization of both the *angular spheroidal functions* $S_{\ell m}(x; c) = {}_0 S_{\ell m}(x; c)$ and the *spin-weighted spherical functions* ${}_s S_{\ell m}(x; 0)$.

The basic symmetries inherent in the spin-weighted spheroidal functions follow from Eq. (4) via the three transformations: $\{s \rightarrow -s, x \rightarrow -x\}$, $\{m \rightarrow -m, x \rightarrow -x, c \rightarrow -c\}$, and complex conjugation. Additional sign and normalization conditions can be chosen for consistency with common sign conventions for the angular-spheroidal and spin-weighted spherical functions. From these, it follows that the spin-weighted spheroidal functions and the separation constants satisfy the following conditions:

$$-_s S_{\ell m}(x; c) = (-1)^{\ell+m} {}_s S_{\ell m}(-x; c), \quad (48a)$$

$${}_s S_{\ell(-m)}(x; c) = (-1)^{\ell+s} {}_s S_{\ell m}(-x; -c), \quad (48b)$$

$${}_s S_{\ell m}^*(x; c) = {}_s S_{\ell m}(x; c^*), \quad (48c)$$

and

$$-_s A_{\ell m}(c) = {}_s A_{\ell m}(c) + 2s, \quad (48d)$$

$${}_s A_{\ell(-m)}(c) = {}_s A_{\ell m}(-c), \quad (48e)$$

$${}_s A_{\ell m}^*(c) = {}_s A_{\ell m}(c^*). \quad (48f)$$

We can expand the spin-weighted spheroidal functions in terms of the spin-weighted spherical functions,

$${}_s S_{\ell m}(x; c) = \sum_{\ell'=\ell_{\min}}^{\infty} C_{\ell' \ell m}(c) {}_s S_{\ell' m}(x; 0), \quad (49)$$

where $\ell_{\min} \equiv \max(|m|, |s|)$. Using this expansion in Eq. (4), and using the fact that

$${}_s A_{\ell m}(0) = l(l+1) - s(s+1), \quad (50)$$

we obtain

$$\begin{aligned} \sum_{\ell'=\ell_{\min}}^{\infty} C_{\ell' \ell m}(c) [\ell'(\ell'+1) - s(s+1) - (cx)^2 \\ + 2csx - {}_s A_{\ell m}(c)] {}_s S_{\ell' m}(x; 0) = 0. \end{aligned} \quad (51)$$

To proceed, we need to remove the x dependence. This can be accomplished using the recurrence relation[34]

$$\begin{aligned} {}_s S_{\ell m}(x; 0) &= \mathcal{F}_{s\ell m} S_{(\ell+1)m}(x; 0) \\ &\quad + \mathcal{G}_{s\ell m} S_{(\ell-1)m}(x; 0) + \mathcal{H}_{s\ell m} S_{\ell m}(x; 0), \end{aligned} \quad (52a)$$

where

$$\mathcal{F}_{s\ell m} = \sqrt{\frac{(\ell+1)^2 - m^2}{(2\ell+3)(2\ell+1)}} \sqrt{\frac{(\ell+1)^2 - s^2}{(\ell+1)^2}}, \quad (52b)$$

$$\mathcal{G}_{s\ell m} = \begin{cases} \text{if } \ell \neq 0 : \sqrt{\frac{\ell^2 - m^2}{4\ell^2 - 1}} \sqrt{\frac{\ell^2 - s^2}{\ell^2}}, \\ \text{if } \ell = 0 : 0, \end{cases} \quad (52c)$$

$$\mathcal{H}_{s\ell m} = \begin{cases} \text{if } \ell \neq 0 \text{ and } s \neq 0 : -\frac{ms}{\ell(\ell+1)}, \\ \text{if } \ell = 0 \text{ or } s = 0 : 0. \end{cases} \quad (52d)$$

For the terms that arise from the x^2 term, we define the following quantities:

$$\mathcal{A}_{s\ell m} = \mathcal{F}_{s\ell m} \mathcal{F}_{s(\ell+1)m}, \quad (53a)$$

$$\mathcal{D}_{s\ell m} = \mathcal{F}_{s\ell m} (\mathcal{H}_{s(\ell+1)m} + \mathcal{H}_{s\ell m}), \quad (53b)$$

$$\mathcal{B}_{s\ell m} = \mathcal{F}_{s\ell m} \mathcal{G}_{s(\ell+1)m} + \mathcal{G}_{s\ell m} \mathcal{F}_{s(\ell-1)m} + \mathcal{H}_{s\ell m}^2, \quad (53c)$$

$$\mathcal{E}_{s\ell m} = \mathcal{G}_{s\ell m} (\mathcal{H}_{s(\ell-1)m} + \mathcal{H}_{s\ell m}), \quad (53d)$$

$$\mathcal{C}_{s\ell m} = \mathcal{G}_{s\ell m} \mathcal{G}_{s(\ell-1)m}. \quad (53e)$$

Using $\mathcal{F}_{s(\ell_{\min}-1)m} = 0$, together with ${}_s S_{(\ell_{\min}-1)m}(x; 0) = {}_s S_{(\ell_{\min}-2)m}(x; 0) = 0$, yields the five-term recurrence relation

$$\begin{aligned} &-c^2 \mathcal{A}_{s(\ell'-2)m} C_{(\ell'-2)\ell m}(c) \\ &- [c^2 \mathcal{D}_{s(\ell'-1)m} - 2cs \mathcal{F}_{s(\ell'-1)m}] C_{(\ell'-1)\ell m}(c) \\ &+ [\ell'(\ell'+1) - s(s+1) - c^2 \mathcal{B}_{s\ell' m} \\ &\quad + 2cs \mathcal{H}_{s\ell' m} - {}_s A_{\ell m}(c)] C_{\ell'\ell m}(c) \\ &- [c^2 \mathcal{E}_{s(\ell'+1)m} - 2cs \mathcal{G}_{s(\ell'+1)m}] C_{(\ell'+1)\ell m}(c) \\ &\quad - c^2 \mathcal{C}_{s(\ell'+2)m} C_{(\ell'+2)\ell m}(c) = 0. \end{aligned} \quad (54)$$

If we truncate the series at $\ell' = \ell_{\max}$ then we have a finite-dimensional spectral approximation to the eigenvalue problem for the spin-weighted spheroidal harmonics. With $N = \ell_{\max} - \ell_{\min} + 1$, then for given values of s and m , we have an $N \times N$ symmetric pentadiagonal matrix \mathbb{M} whose elements are given by

$$M_{\ell\ell'} = \begin{cases} \text{if } \ell' = \ell - 2 : -c^2 \mathcal{A}_{s\ell' m}, \\ \text{if } \ell' = \ell - 1 : -c^2 \mathcal{D}_{s\ell' m} + 2cs \mathcal{F}_{s\ell' m}, \\ \text{if } \ell' = \ell : {}_s A_{\ell' m}(0) - c^2 \mathcal{B}_{s\ell' m} + 2cs \mathcal{H}_{s\ell' m}, \\ \text{if } \ell' = \ell + 1 : -c^2 \mathcal{E}_{s\ell' m} + 2cs \mathcal{G}_{s\ell' m}, \\ \text{if } \ell' = \ell + 2 : -c^2 \mathcal{C}_{s\ell' m}, \\ \text{otherwise} : 0. \end{cases} \quad (55)$$

The truncated version of Eq. (54) is then simply the eigenvalue equation

$$\mathbb{M} \cdot \vec{C}_{\ell m}(c) = {}_s A_{\ell m}(c) \vec{C}_{\ell m}(c). \quad (56)$$

For given s , m , and c , the matrix \mathbb{M} is constructed and its N eigenvalues are the ${}_s A_{\ell m}(c)$, where $\ell \in \{\ell_{\min}, \dots, \ell_{\max}\}$, and the elements of the corresponding eigenvector $\vec{C}_{\ell m}(c)$ are the expansion coefficients $C_{\ell'\ell m}(c)$.

Because of the exponential convergence of spectral expansions, for $\ell \geq \ell_{\min}$ but $\ell \ll \ell_{\max}$, we expect ${}_s A_{\ell m}(c)$ and $\vec{C}_{\ell m}(c)$ to have extremely high accuracy. The largest value of ℓ for which we can expect an accurate eigenvalue and eigenvector can be determined by looking at the resulting values of the expansion coefficients $C_{\ell'\ell m}(c)$. For given ℓ and m , only coefficients where ℓ' is reasonably close to ℓ will have significant weight. As long as the coefficients $C_{\ell'\ell m}(c)$ are negligible for $\ell' \geq \ell_{\max}$, then the solution associated with ${}_s A_{\ell m}(c)$ will be highly accurate.

In practice, given values for s , m , and c we choose a value for N and solve the eigenvalue problem of Eq. (56) for its N eigenvalues and associated eigenvectors. While many of these eigensolutions will be accurate, we are typically only interested in the solution associated with a particular value of ℓ . What is meant by the ℓ th eigenvalue is not uniquely defined. For $c = 0$, the eigenvalues ${}_s A_{\ell m}(0)$ increase monotonically with ℓ . While this is a logical choice, it is simply a labeling scheme. We choose to identify the ℓ th eigenvalue via continuity along some sequence of solutions connected to the well-defined value of ${}_s A_{\ell m}(0)$. In practice, this means that we also need the eigenvalue ${}_s A_{\ell m}(c - \epsilon)$ from a neighboring solution along a sequence. Here, ϵ is complex but $|\epsilon|$ is small. Then, we choose the eigenvalue ${}_s A_{\ell m}(c)$ as the element, from the set of eigenvalues, that minimizes $|{}_s A_{\ell m}(c) - {}_s A_{\ell m}(c - \epsilon)|$. The necessity of picking one solution from a set of possible solutions is not unique to this new spectral method for solving Eq. (4). Rather, it is common to all methods.

In order to determine if the solution is accurate, we examine the eigenvector, $\vec{C}_{\ell m}(c)$, associated with the chosen eigenvalue. The elements, $C_{\ell'\ell m}(c)$, of $\vec{C}_{\ell m}(c)$ are indexed by the spin-weighted *spherical* function index ℓ' . When ℓ' is close to the value of the *spheroidal* label ℓ , the coefficients will have significant weight. However, once the number of values of ℓ' used becomes sufficiently large (the convergent regime) then $|C_{\ell'\ell m}(c)|$ will decrease exponentially with increasing ℓ' . In practice, once a solution is obtained, we determine $|C_{\ell'\ell m}(c)|$ with $\ell' = \ell_{\max}$ and demand that it be smaller than some tolerance. If it is not, we increase N and repeat the process. Because of exponential convergence, the magnitude of this last element of $\vec{C}_{\ell m}(c)$ places a robust upper bound on the error of the solution.

If the spin-weighted spheroidal eigenfunctions are needed, we must fix their phase and normalization. These are fixed by the corresponding spin-weighted spherical function at $c = 0$. To fix the phase of the solutions, we demand that $C_{\ell'\ell m}(c)$ with $\ell' = \ell$ is real. To maintain proper normalization, we enforce $\sum_{\ell'=l_{\min}}^{\ell_{\max}} |C_{\ell'\ell m}(c)|^2 = 1$.

This spectral eigenvalue approach for solving Eq. (4) has several clear advantages over approaches that use one

of the variants of Leaver's method. Compared to an expansion in terms of powers of $(1 + x)$ used in the traditional Leaver approach, the size of the matrix N is vastly smaller than the number of terms required in the continued fraction in order to determine the eigenvalue with high accuracy. The use of an expansion in terms of Jacobi polynomials provides a significant improvement. This is easily seen because the spin-weighted spherical functions are proportional to the Wigner d function $d_{mn}^\ell(\theta)$ which itself is the product of powers of both $\cos \frac{\theta}{2}$ and $\sin \frac{\theta}{2}$, and a Jacobi polynomial. However, the expansion in terms of spin-weighted spherical functions is still more efficient. More importantly, very sophisticated tools exist for solving matrix eigenvalue problems and these can be used with the spectral eigenvalue approach to simultaneously yield both the desired eigenvalue and the coefficients of the series expansion of the spin-weighted spheroidal function. When the expansion coefficients are required for a solution based on one of the variants of Leaver's method, it is important to remember that it is a *minimal* solution that is being constructed. Care must be taken in constructing the coefficients so that a dominant solution is not found instead.

The size of the matrix needed in order to meet a given tolerance tends to increase with both c and ℓ . For the QNM examples we have considered, in the extreme Kerr limit of $a \rightarrow M$ and values of ℓ up to 12, achieving a tolerance of 10^{-14} required a matrix no larger than $N = 25$. Figure 1 displays the behavior of the spectral expansion coefficients, $C_{\ell'\ell m}(c)$, for two representative examples. The upper plot of Fig. 1 corresponds to the fundamental mode of $\ell = 2$, $m = 2$. In this case, $\ell' = 2, \dots, 6$ for small \bar{a} , and $\ell' = 2, \dots, 14$ in the extreme limit. Along the curve for each ℓ' , \bar{a} varies from 0 to nearly 1, and $c = \bar{a}\bar{\omega}$ where $\bar{\omega}$ is the complex QNM frequency for this mode, the value of which also depends on \bar{a} . The vertical axis gives the base-10 log of $|C_{\ell'\ell m}(c)|$. We can clearly see that $C_{220}(c)$ contains the dominant amount of spectral power in this case, and that the convergence of the expansion is exponential as ℓ' increases. The lower plot of Fig. 1 corresponds to the fundamental mode of $\ell = 6$, $m = 2$. In this case, $\ell' = 2, \dots, 10$ for small \bar{a} , $\ell' = 2, \dots, 19$ in the extreme limit, and it is $C_{660}(c)$ that contains the dominant amount of spectral power in the expansion. Again, we can see the exponential falloff in the importance of the other spectral elements as $|\ell' - \ell|$ increases.

III. QNMS OF KERR

As discussed in Sec. II A, to compute the QNMs of Kerr requires that we find a solution of the coupled angular and radial Teukolsky equations, Eqs. (4) and (5a). For given ℓ and m , there are an infinite number of solutions to the coupled equations. These correspond to the fundamental mode and its overtones, labeled by the overtone index n . At $\bar{a} = 0$, the fundamental mode has

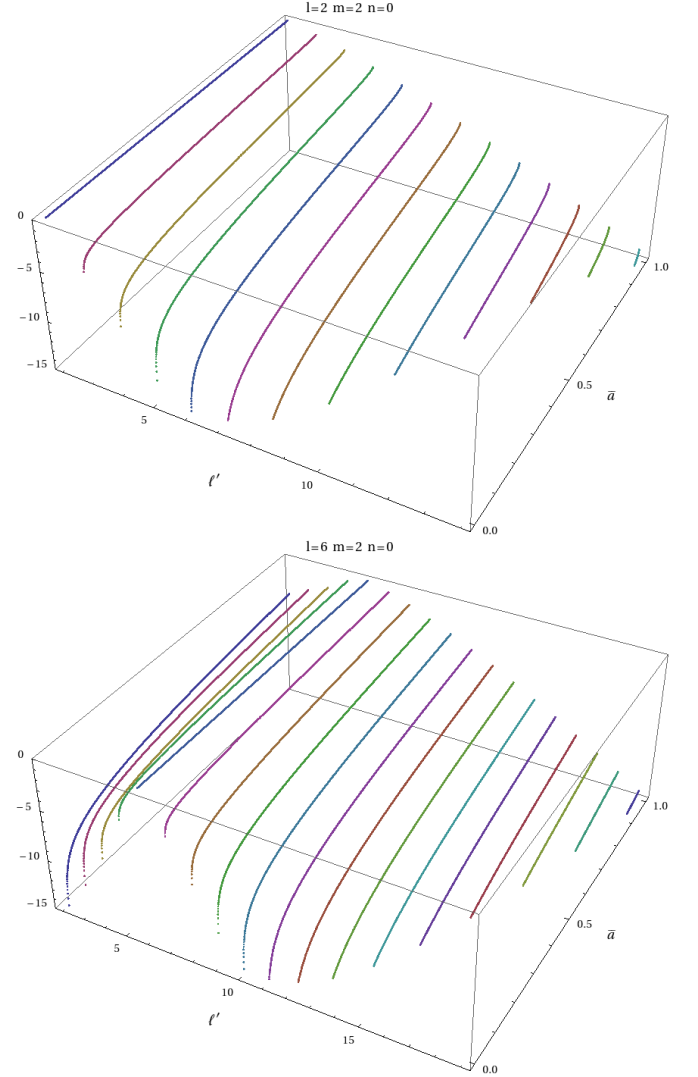


FIG. 1. Magnitude of the spectral coefficients $C_{\ell'\ell m}(c)$ along Kerr QNM sequences. Each line plots $\log |C_{\ell'\ell m}(c)|$, for a particular ℓ' and with $c = \bar{a}\bar{\omega}$ along a particular QNM sequence with $0 \leq \bar{a} < 1$. The upper plot shows the coefficient of the fundamental mode for $\ell = 2$, $m = 2$ (see Fig. 3). The lower plot shows the coefficients of the fundamental mode for $\ell = 6$, $m = 2$ (see Fig. 9).

the slowest decay rate [smallest $|\text{Im}(\bar{\omega})|$] and is labeled $n = 0$. The overtones are labeled by increasing values for n in order of successively faster decay rates at $\bar{a} = 0$. At sufficiently large values of \bar{a} , this ordering can change, but we maintain the overtone index at $\bar{a} = 0$ along a QNM sequence as \bar{a} increases.

The QNM spectrum is thus labeled by the triplet $\{\ell, m, n\}$ and the complex frequency is a function of \bar{a} . Because of a fundamental symmetry to the equations, the Kerr QNM spectrum has two distinct sets of modes for any given value of \bar{a} : the “positive-frequency” modes $\bar{\omega}_{\ell mn}$ with $|\text{Re}(\bar{\omega})| \geq 0$, and the “negative-frequency” modes $\bar{\omega}'_{\ell mn}$. The two sets are directly related to each

other by

$$\bar{\omega}'_{\ell mn}(\bar{a}) = -\bar{\omega}_{\ell(-m)n}^*(\bar{a}). \quad (57)$$

The corresponding separation constants are related by

$${}_s A'_{\ell m}(\bar{a}\bar{\omega}'_{\ell mn}) = {}_s A_{\ell(-m)}^*(\bar{a}\bar{\omega}_{\ell(-m)n}). \quad (58)$$

Because of this symmetry, it is only necessary to compute either the positive- or negative-frequency modes. We will always compute the positive-frequency modes.

In general, computation of these modes must be done numerically via an iterative process. The routines to do this were coded in **Mathematica** in order to make use of its ability to perform extended precision arithmetic. Calculations were performed using 24 decimal digit precision (as opposed to the 16 digits of machine precision). In a few cases where even higher precision might be required, we have used up to 32 digit precision.

In this paper, we will be concerned primarily with gravitational modes so that $s = -2$; however the methods we discuss apply to any fixed value of s . For a given triplet $\{\ell, m, n\}$, a “mode sequence” consists of computing the complex frequency $\bar{\omega}_{\ell mn}(\bar{a})$, the separation constant ${}_s A_{\ell m}(\bar{a}\bar{\omega}_{\ell mn})$, and a set (indexed by ℓ') of spectral coefficients $C_{\ell' \ell m}(\bar{a}\bar{\omega}_{\ell mn})$ for $0 \leq \bar{a} < 1$. A mode sequence is computed by providing initial guesses for $\bar{\omega}_{\ell mn}(\bar{a})$ and ${}_s A_{\ell m}(\bar{a}\bar{\omega}_{\ell mn})$. We almost always start with $\bar{a} = 0$, using values for the QNMs of Schwarzschild. Given a solution at this value of \bar{a} we increase \bar{a} by at most 10^{-3} and use the previous solution as an initial guess for the next. When possible, we use quadratic extrapolation based on three previous solutions to compute a more accurate initial guess. We use an adaptive step-size approach to ensure we resolve fine details in the sequence, allowing steps as small as 10^{-6} in general. However, in order to explore the behavior near $\bar{a} = 1$, we use step sizes as small as 10^{-9} .

Each element in a mode sequence is computed, starting with an initial guess for $\bar{\omega}_{\ell mn}(\bar{a})$ and ${}_s A_{\ell m}(\bar{a}\bar{\omega}_{\ell mn})$, by finding simultaneous solutions of the angular and radial Teukolsky equations, Eqs. (4) and (5a). The angular equation is solved using the spectral eigenvalue approach outlined in Sec. II D 1 using the **Mathematica** routine **Eigensystem** to obtain the eigenvalues and eigenvectors of the matrix. The size of the matrix is at least $N = 4$, but is chosen dynamically. The radial equation is solved using the continued fraction method outlined in Sec. II C 1. The desired root of the continued fraction $Cf(n; N) = 0$ [see Eq. (44)] is located using a two-dimensional Newton iteration with numerical derivatives. The “inversion” number of the continued fraction is set to the overtone index n , and the truncation number N is at least 300, but is chosen dynamically.

An iterative approach is needed for solving the coupled pair of equations. The most common approach would be to solve the radial equation for $\bar{\omega}$ holding ${}_s A_{\ell m}(\bar{a}\bar{\omega})$ fixed at the value from the previous solution of the angular equation. Then the angular equation is solved for

${}_s A_{\ell m}(\bar{a}\bar{\omega})$ holding $\bar{\omega}$ fixed from its previous solution. For most cases, an iterative approach of this sort works well, but convergence to a solution is not guaranteed. In fact, there are situations where convergence is very slow, or even fails unless some sort of “underrelaxation” is used. We have even encountered extreme situations where no amount of underrelaxation could achieve convergence. The source of the convergence problem, and its solution, can be seen by considering the details of Newton’s method used to solve the radial equation.

Newton’s method requires that we evaluate the derivative of the function whose root we are seeking[31]. In our case, this is done numerically via finite differencing. The continued-fraction equation derived from the radial equation is a function of both the complex frequency $\bar{\omega}$ and the angular separation constant ${}_s A_{\ell m}(\bar{a}\bar{\omega})$ which is itself a function of $\bar{\omega}$. The derivative of the continued fraction equations has the form

$$\frac{\partial f(\bar{\omega}, A)}{\partial \bar{\omega}} + \frac{\partial f(\bar{\omega}, A)}{\partial A} \frac{\partial A}{\partial \bar{\omega}}. \quad (59)$$

During a standard iterative approach, where ${}_s A_{\ell m}(\bar{a}\bar{\omega})$ is held fixed, the second term in Eq. (59) is ignored. If this term is small, then it should not significantly affect the convergence of the Newton iteration for the root of the continued fraction, and it may not spoil the iterative convergence of the coupled equations. However, if this term is not small, then it can degrade the convergence of the Newton iterations, and can spoil the convergence of the iterative solution of the coupled equations.

The iterative convergence problem is solved by effectively including this second term when computing the numerical derivatives of the radial continued-fraction equation. Our numerical derivatives are computed by evaluating the continued-fraction equation at neighboring values of $\bar{\omega}$. Since $\bar{\omega}$ is complex, we must compute derivatives with step $\delta\bar{\omega}$ both purely real and purely imaginary. Prior to evaluating the radial continued-fraction equation for any value of $\bar{\omega}$, the angular equation is solved with that value for $\bar{\omega}$. The derivatives are then evaluated as

$$\frac{f(\bar{\omega} + \delta\bar{\omega}, A(a(\bar{\omega} + \delta\bar{\omega}))) - f(\bar{\omega}, A(a\bar{\omega}))}{\delta\bar{\omega}}. \quad (60)$$

In this way, the coupled equations are solved simultaneously during the Newton iteration process for finding the root of the radial continued-fraction equation. This process involves solving the angular eigenvalue problem three times during each Newton iteration, but solving the angular problem is fast in practice compared to each evaluation of the radial continued fraction.

Once a root for the radial equation has been found, both the matrix size and the continued fraction truncation length are checked to make sure they provide sufficient accuracy. If not, these are increased and the entire process is repeated.

For the results discussed in this paper, sufficiently high precision and sufficiently small tolerances have been used

that we can expect our results to have an absolute accuracy of at least 10^{-10} . This is a conservative estimate based on the possibility of pathological cases such as the continued fraction equation having small derivatives local to the root. In general, we expect an absolute accuracy of $\sim 10^{-12}$.

A. The gravitational QNMs

We have performed an extensive, high-accuracy survey of the gravitational ($s = -2$) QNMs of Kerr for $2 \leq \ell \leq 12$, $-\ell \leq m \leq \ell$, and $0 \leq n \leq 7$. In addition we have computed the mode sequences for $n = 8$ with $\ell = 2$ and $-2 \leq m \leq 2$. Many of the results covered in this set have been computed and discussed in the past[5, 8, 28]. We will not attempt to display all of these results. We will display some representative examples, particularly interesting mode sequences, and enough detail to allow our results to be confirmed. We will then turn to a detailed exploration of two interesting problems: the extremal limit, and zero-frequency modes.

We begin with Fig. 2 which displays the complex frequencies $\bar{\omega}$ for all mode sequences with $m = 2$. The plot is rather dense but provides a useful overview of the $m = 2$ modes. We note that in all plots of $\bar{\omega}$, we invert the imaginary axis. Beginning on the left side of the figure, we find eight sequences connected by a dashed line. We will denote individual mode sequences by their triplet $\{\ell, m, n\}$. The bottommost sequence on the left is $\{2, 2, 0\}$. The topmost sequence on the left is $\{2, 2, 7\}$. Between them, in order going up the figure, are the $n = 1-6$ modes. The dashed line connecting these eight mode sequences passes through the $\bar{a} = 0$ mode of each sequence and \bar{a} increase along each sequence as it extends from this point. The markers along each sequence denote an increase in \bar{a} of 0.05. The last marker, on each sequence appears at $\epsilon \equiv 1 - \bar{a} = 10^{-6}$ for most sequences, but for sequences that approach the real axis, it is at $\epsilon = 10^{-8}$. Just to the right of the $\ell = 2$ modes are the $\ell = 3$ modes. Again for each n , the $\bar{a} = 0$ modes are connected by a dashed line. Proceeding sequentially to the right we find the remaining $\ell = 4-12$ mode sequences.

The left plot in Fig. 3 shows the $\{2, 2, n\}$ modes in isolation. The sequences in this figure are exactly as described above. The right plot shows the corresponding sequences for the separation constant ${}_{-2}A_{22}(\bar{a}\bar{\omega}_{22n})$. All ${}_{-2}A_{\ell m}()$ sequences begin on the real axis at $\ell(\ell+1) - 2$. In the neighborhood of this point, the overtone index n of each sequence increases as we move to a new sequence in a clockwise direction. Markers along these sequences are at the same values of \bar{a} as their $\bar{\omega}$ counterparts.

Notice that all of the mode sequences, except $n = 5$, approach an accumulation point at $\bar{\omega} = m/2$. This behavior is well known, studied by Detweiler[16] and others[17–19, 27, 35]. As the mode sequences approach the real axis, the decrease in the imaginary part of $\bar{\omega}$ corresponds to a decrease in the mode damping rate. We will

consider these accumulation points in more detail below. There is no clear understanding yet of why some modes, like $\{2, 2, 5\}$ break the trend of neighboring modes. As seen in Fig. 4, the anomalous behavior is not a cusp, but rather a loop. The behavior of this mode was first described by Leaver[5].

The plots in Fig. 5 show the $\{3, 2, n\}$ modes in isolation. In contrast to the $\{2, 2, n\}$ modes, we note that the $\{3, 2, 0\}$ sequence does not approach the accumulation point at $\bar{\omega} = m/2$. However, all of the displayed sequences with $n \geq 1$ do approach this accumulation point. We see similar behavior in Fig. 6 which shows the $\{4, 2, n\}$ mode sequences in isolation. In this case, the first three sequences ($n = 0, 1$, and 2) do not approach the accumulation point. Sequences with higher overtones do approach the accumulation point with the exception of $n = 6$. As seen in Fig. 7, this anomalous sequence terminates with finite damping after executing a number of spirals. Finally, Figs. 8 and 9 show, respectively, the $\{5, 2, n\}$ and $\{6, 2, n\}$ mode sequences in isolation. For $\ell = 5$, the sequences with $n = 0-5$ do not approach the accumulation point while the last two do. For $\ell = 6$, none of the displayed sequences approach the accumulation point. However, we do expect that mode sequences with high enough overtone numbers will terminate at the accumulation point.

Figure 10 displays all mode sequences for $m = 1$. Again, we see an accumulation point at $m/2$. Mode sequences for $\{2, 1, n\}$ and $\{3, 1, n\}$ are displayed in isolation, respectively, in Figs. 11 and 12. For $\ell = 2$, we see that the $n = 0$ and 1 overtones do not approach the accumulation point, while all subsequent displayed sequences do terminate there. For $\ell = 3$, the $n = 0-3$ do not approach the accumulation point, the next two do approach it, but $n = 6$ terminates at finite damping following several spirals. The end of the $\{3, 1, 6\}$ sequence is shown in Fig. 13.

Figure 14 displays all mode sequences for $m = 0$, and Fig. 15 displays the $\{2, 0, n\}$ mode sequences in isolation. None of the sequences shown approach an accumulation point at 0, and indeed accumulation points are only expected for $m > 0$ for positive-frequency modes. For $\ell = 2$, the $n = 5-7$ mode sequences terminate in the unusual oscillation or spiraling seen previously in Figs. 4, 7, and 13. The termination of the $\{2, 0, 5-7\}$ sequences are shown in Fig. 16. We also note that these examples display the most dramatic oscillatory effects in the separation constant ${}_{-2}A_{20}(\bar{a}\bar{\omega}_{20n})$ as seen in Fig. 15.

The final two mode sets we show are for $m = -1$ and $m = -2$. Figures 17 and 18 display all modes for these two sets. The complex frequencies for modes with $m < 0$ never approach an accumulation point on the positive real axis. Recall, however, that the behavior we have displayed is for the positive-frequency modes. There also exists the second set of QNMs, see Eq. (57), for which $\text{Re}(\bar{\omega}) < 0$. For these negative-frequency modes, it is the modes with $m < 0$ that can approach an accumulation point at $m/2$.

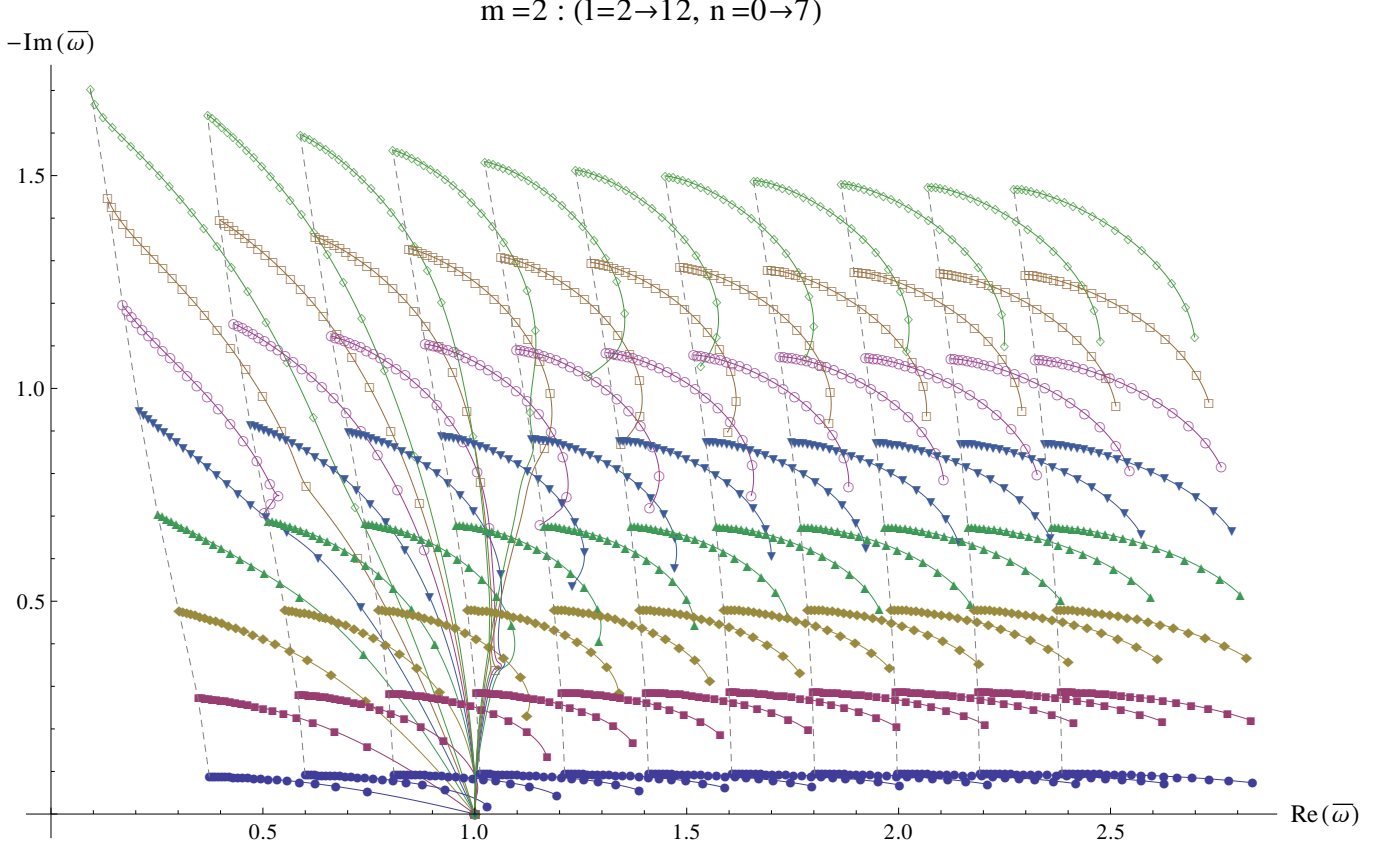


FIG. 2. Kerr QNM mode sequences for $m = 2$. The complex frequency $\bar{\omega}$ is plotted for the cases $\ell = 2 \rightarrow 12$ and $n = 0 \rightarrow 7$. Note that the imaginary axis is inverted. Each sequence covers the range $0 \leq \bar{a} < 1$, with markers on each sequence denoting a change in \bar{a} of 0.05. The $\bar{a} = 0$ element of each set of mode sequences with the same ℓ are connected by a dashed line. ℓ increases monotonically as we move to the right in the plot. The overtone index n for each set of modes with the same ℓ increases monotonically as we move up along each dashed line.

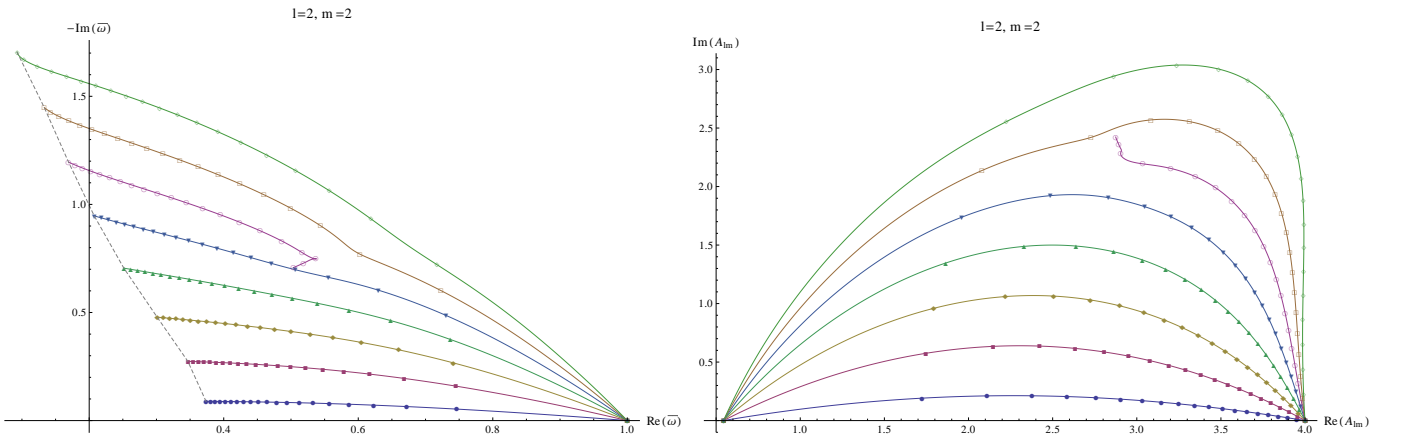


FIG. 3. Kerr QNM mode sequences for $\ell = 2$ and $m = 2$. The left plot displays the complex frequency $\bar{\omega}$ and the right plot displays the separation constant ${}_{-2}A_{22}(\bar{a}\bar{\omega}_{22n})$ for corresponding mode sequences. The left plot is as described in the caption for Fig. 2. For the right plot, each sequence begins with $\bar{a} = 0$ on the real axis at $\ell(\ell + 1) - 2$. The overtones all radiate from this point with n increasing in a clockwise direction. $n = 0 \rightarrow 7$ are displayed for both plots.

1. The extremal limit

Examining Figs. 2 and 10, the most striking feature in each plot is the accumulation point at $\bar{\omega} = m/2$

for the extreme limit of many of the sequences. While we do not show all of the figures, this behavior is seen for all of the sets of positive-frequency mode sequences

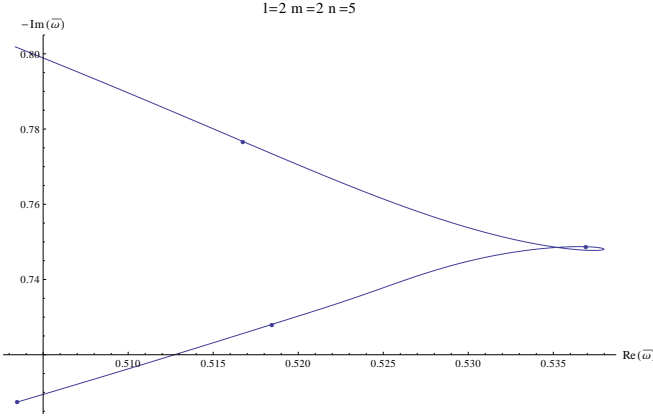


FIG. 4. Close-up of $\bar{\omega}$ for the $\{2, 2, 5\}$ sequence showing the unusual termination of this sequence. Instead of approaching the accumulation point at $m/2$, this sequence makes a sharp loop and then terminates with finite damping. See Fig. 3 for context.

[ie $\text{Re}(\bar{\omega}) \geq 0$] with $m > 0$ that we have constructed. By symmetry, these accumulation points will also occur for the negative-frequency mode sequences with $m < 0$. This behavior was first predicted by Detweiler[16]. His analysis was extended and amended by Cardoso[17] and Hod[27], yielding an approximation for $\bar{\omega}$ in the limit as $\bar{a} \rightarrow 1$. Recently, these modes have been studied extensively by Yang *et al*[18, 19]. Using matched asymptotic expansions, they derived a formula for $\bar{\omega}$ in the extreme limit when the solutions approach an accumulation point.

They find

$$\bar{\omega} \approx \frac{m}{2} - \delta \sqrt{\frac{\epsilon}{2}} - i \left(\tilde{n} + \frac{1}{2} \right) \sqrt{\frac{\epsilon}{2}}, \quad (61)$$

where $\epsilon \equiv 1 - \bar{a}$, \tilde{n} indexes over the set of overtones that approach the accumulation point, and

$$\delta^2 \equiv \frac{7m^2}{4} - \left(s + \frac{1}{2} \right)^2 - {}_{-2}A_{\ell m}(m/2). \quad (62)$$

Equation (61) is supposed to be a good approximation for $\bar{\omega}$ except for cases where $|\delta| \sim 1$ and for a small range of $\delta^2 < 0$ (see Ref. [19]).

When the angular Teukolsky equation (4) is solved for real c , the separation constant ${}_sA_{\ell m}(c)$ is real, meaning that δ^2 is real. This means that δ will either be real or pure imaginary, which corresponds to the two types of behavior seen in the mode sequences that approach the accumulation points at $\bar{\omega} = m/2$. Figure 3, showing the case $\{2, 2, n\}$, illustrates the behavior when $\delta^2 > 0$. In this case, all of the modes (except for exceptional case of $n = 5$) approach the accumulation point. The fitting overtone index \tilde{n} in Eq. (61) takes on consecutive values starting at zero, so that in this case the set $n \in \{0, 1, 2, 3, 4, 6, 7\}$ maps to $\tilde{n} \in \{0, 1, 2, 3, 4, 5, 6\}$. Figures 5, 6, and 8, showing the cases $\{3-5, 2, n\}$, illustrate the behavior when $\delta^2 < 0$. In these cases, we see

that the first few overtones approach a finite value for the $\text{Im}(\bar{\omega})$ in the extremal limit, and then the remaining overtones (except for exceptional cases) approach the accumulation point. For example, in Fig. 6 we find that the overtones $n \in \{3, 4, 5, 7\}$ approach the accumulation point. In this case, the fitting overtone index takes on the values $\tilde{n} \in \{0, 1, 2, 3\}$.

For those mode sequences that approach an accumulation point in the extremal limit, we have extended the sequence in decadal steps down to $\epsilon = 10^{-8}$ (except for $\{4, 3, n\}$ where $\epsilon = 10^{-9}$) and compared our results with Eq. (61) finding very good agreement. In fact, we have fit our results to a version of Eq. (61) that has been extended to next to leading order behavior in ϵ . We have also constructed fitting functions for the separation constant ${}_{-2}A_{\ell m}(\bar{a}\bar{\omega})$. These extended fitting functions must be defined independently for the cases when $\delta^2 > 0$ and $\delta^2 < 0$.

The fitting functions for the case $\delta^2 > 0$ are given in Eqs. (63). The real and imaginary parts of $\bar{\omega}$ are fit using Eqs. (63a) and (63b).

$$\text{Re}[\bar{\omega}] = \frac{m}{2} - \alpha_1 \sqrt{\frac{\epsilon}{2}} + (\alpha_2 + \alpha_3 \tilde{n}) \epsilon \quad (63a)$$

$$\text{Im}[\bar{\omega}] = - \left(\tilde{n} + \frac{1}{2} \right) \left(\sqrt{\frac{\epsilon}{2}} - \alpha_4 \epsilon \right) \quad (63b)$$

$$\text{Re}[{}_sA_{\ell m}] = \ell(\ell+1) - s(s+1) + \beta_1 \quad (63c)$$

$$+ \beta_2 \sqrt{\frac{\epsilon}{2}} + (\beta_3 + \beta_4 \tilde{n} + \beta_5 \tilde{n}^2) \epsilon$$

$$\text{Im}[{}_sA_{\ell m}] = \left(\tilde{n} + \frac{1}{2} \right) \left(\beta_6 \sqrt{\frac{\epsilon}{2}} + \beta_7 \epsilon \right) \quad (63d)$$

Comparing to Eq. (61), we see that our coefficient α_1 should correspond to δ . The coefficients α_2 , α_3 , and α_4 are associated with the next to leading order behavior in ϵ . The real and imaginary parts of ${}_{-2}A_{\ell m}(\bar{a}\bar{\omega})$ are fit using Eqs. (63c) and (63d). For the separation constant, the coefficients β_2 and β_6 are associated with the leading order behavior in ϵ . The coefficient β_1 defines the limiting behavior ${}_{-2}A_{\ell m}(m/2) = \ell(\ell+1) - 2 + \beta_1$, required in Eq. (62) to determine the value of δ^2 . The remaining coefficients β_3 , β_4 , β_5 , and β_7 are associated with its next to leading order behavior for the separation constant.

The fit values for all cases with $\delta^2 > 0$ are shown in Tables I and II. The fitted values shown in these tables are displayed to six significant digits unless the fit yielded fewer significant digits. In this case, the result is shown to its last significant digit along with the one-sigma error in this last digit in parentheses. The excellent agreement of our results with Eq. (61) is seen in the agreement between δ and α_1 in Table I. The largest discrepancy is seen for the case $\ell = 5$, $m = 4$ where the results only agree to three significant figures. But, in this case, $\delta \sim 1.07$ and we recall that Eq. (61) was not claimed to be a good approximation when $|\delta| \sim 1$. Nevertheless, the agreement is still quite good, and we note the clear tendency for the accuracy of all fit parameters to increase with increasing

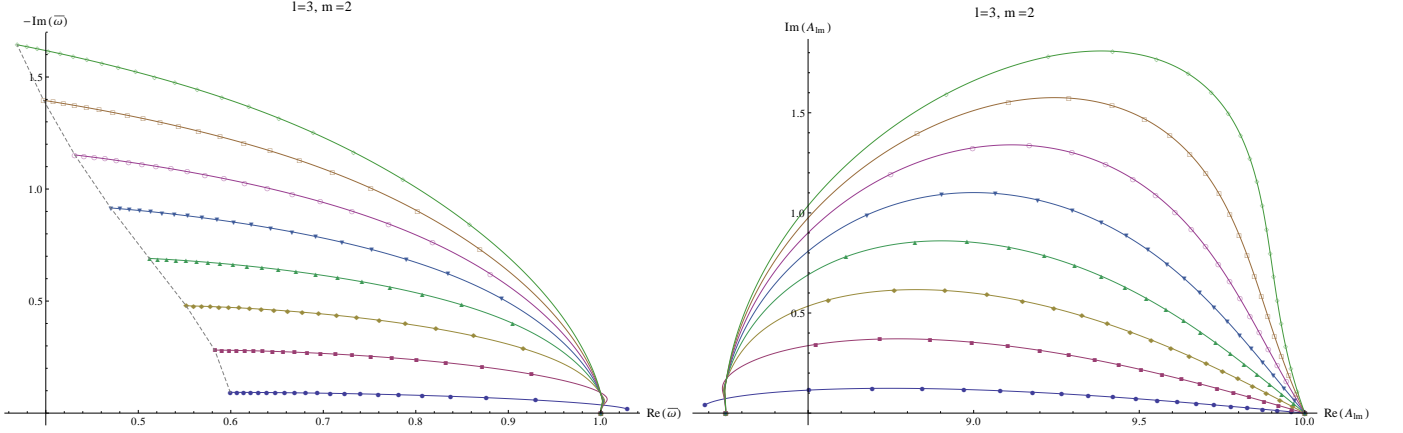


FIG. 5. Kerr QNM mode sequences for $\ell = 3$ and $m = 2$. Plots are as described in Fig. 3.

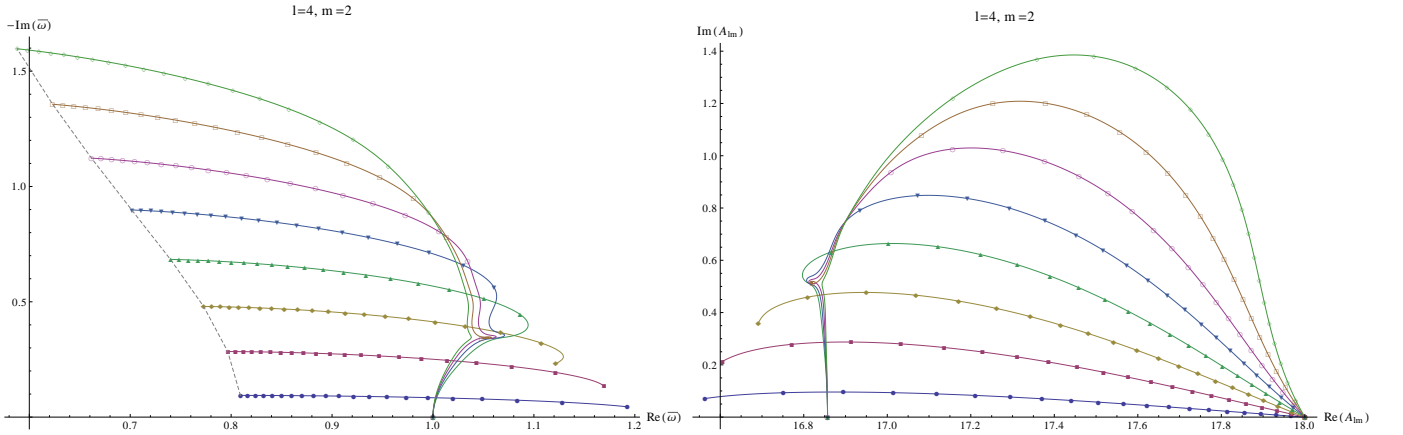


FIG. 6. Kerr QNM mode sequences for $\ell = 4$ and $m = 2$. Plots are as described in Fig. 3.

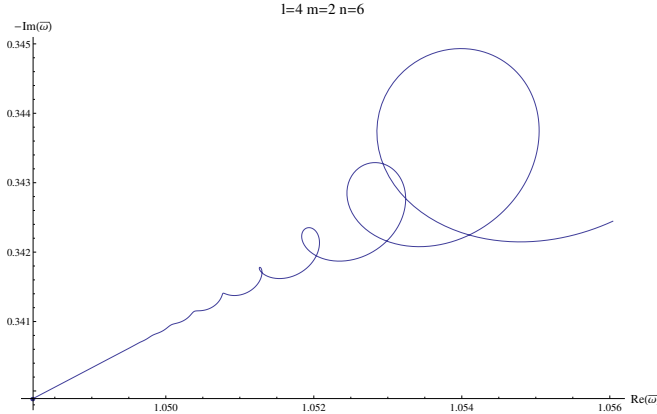
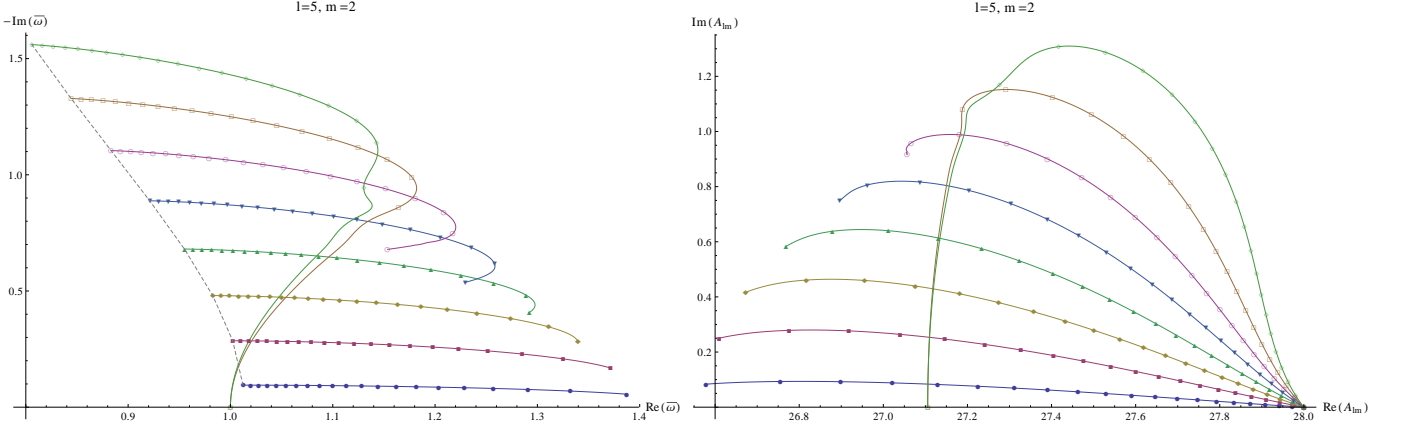
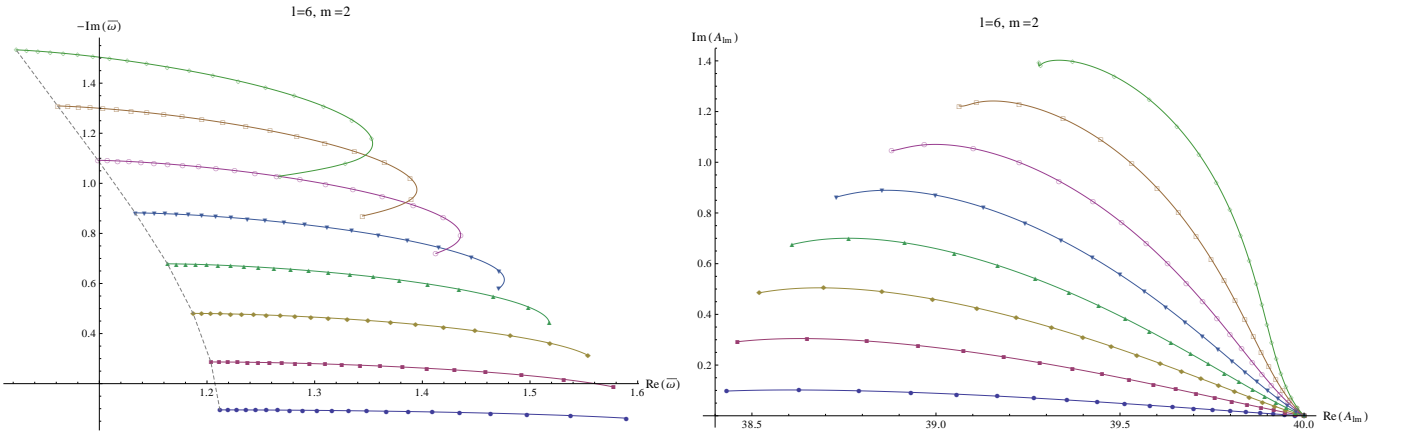


FIG. 7. Close-up of $\bar{\omega}$ for the $\{4, 2, 6\}$ sequence showing the unusual termination of this sequence. See Fig. 6 for context.

δ . The plots in Fig. 19 show the quality of the fit in the worst case, $\ell = 5$ and $m = 4$. The dependence of the fit to the overtone index occurs at leading order in ϵ for $\text{Im}(\bar{\omega})$ and is clearly seen in the right plot of Fig. 19; however its dependence in the real part occurs only at next to

leading order and is barely visible in the left plot. However, the next to leading order behavior in ϵ is important for all cases. To illustrate this, we have also plotted the fit curves omitting the terms at next to leading order in ϵ . The \tilde{n} dependence in $\text{Re}(\bar{\omega})$ is represented in the α_3 coefficient and we see that its significance is strongly dependent on δ , increasing with increasing δ . For the case plotted in Fig. 19, an even higher-order term with quadratic dependence on \tilde{n} appears to be important. In fact, there is evidence for such a term in all of our fits; however we have not tried to find a fit with additional terms.

Table II and Fig. 20 show the results for fitting the real and imaginary parts of ${}_{-2}A_{\ell m}(\bar{a}\bar{\omega})$ using Eqs. (63c) and (63d). We see that the leading order behavior of $\text{Im}_{(s)}A_{\ell m}$ is proportional to the leading order behavior of $\text{Im}(\bar{\omega})$, including its dependence on \tilde{n} . The same is true for the next to leading order behavior, although the proportionality constant is different for the two terms. As with $\bar{\omega}$, all of the \tilde{n} dependence in the real part of ${}_{-2}A_{\ell m}(\bar{a}\bar{\omega})$ occurs in the next to leading order term, and as can be seen in the left plot of Fig. 20 is barely visible. The coefficients β_4 and β_5 encode this depen-

FIG. 8. Kerr QNM mode sequences for $\ell = 5$ and $m = 2$. Plots are as described in Fig. 3.FIG. 9. Kerr QNM mode sequences for $\ell = 6$ and $m = 2$. Plots are as described in Fig. 3.

dence on the overtone index and their significance is again strongly correlated with the magnitude of δ . Interestingly, for larger values of δ , where these coefficients are determined with several significant figures, it seems clear that $\beta_4 = \beta_5$, so the dependence on the overtone index is proportional to $\tilde{n}(\tilde{n} + 1)$ [or to $(\tilde{n} + 1)^2$ with a redefinition of β_3]. Only the case $\ell = 5, m = 4$ (where $\delta \sim 1.07$) seems to violate this scaling.

The fitting functions for the case $\delta^2 < 0$ are given in Eqs. (64). The real and imaginary parts of $\bar{\omega}$ are fit using Eqs. (64a) and (64b):

$$\text{Re}[\bar{\omega}] = \frac{m}{2} + (\alpha_1 + \alpha_2 \tilde{n}) \epsilon \quad (64a)$$

$$\text{Im}[\bar{\omega}] = - \left(\alpha_3 + \tilde{n} + \frac{1}{2} \right) \sqrt{\frac{\epsilon}{2}} + (\alpha_4 + \alpha_5 \tilde{n}) \epsilon \quad (64b)$$

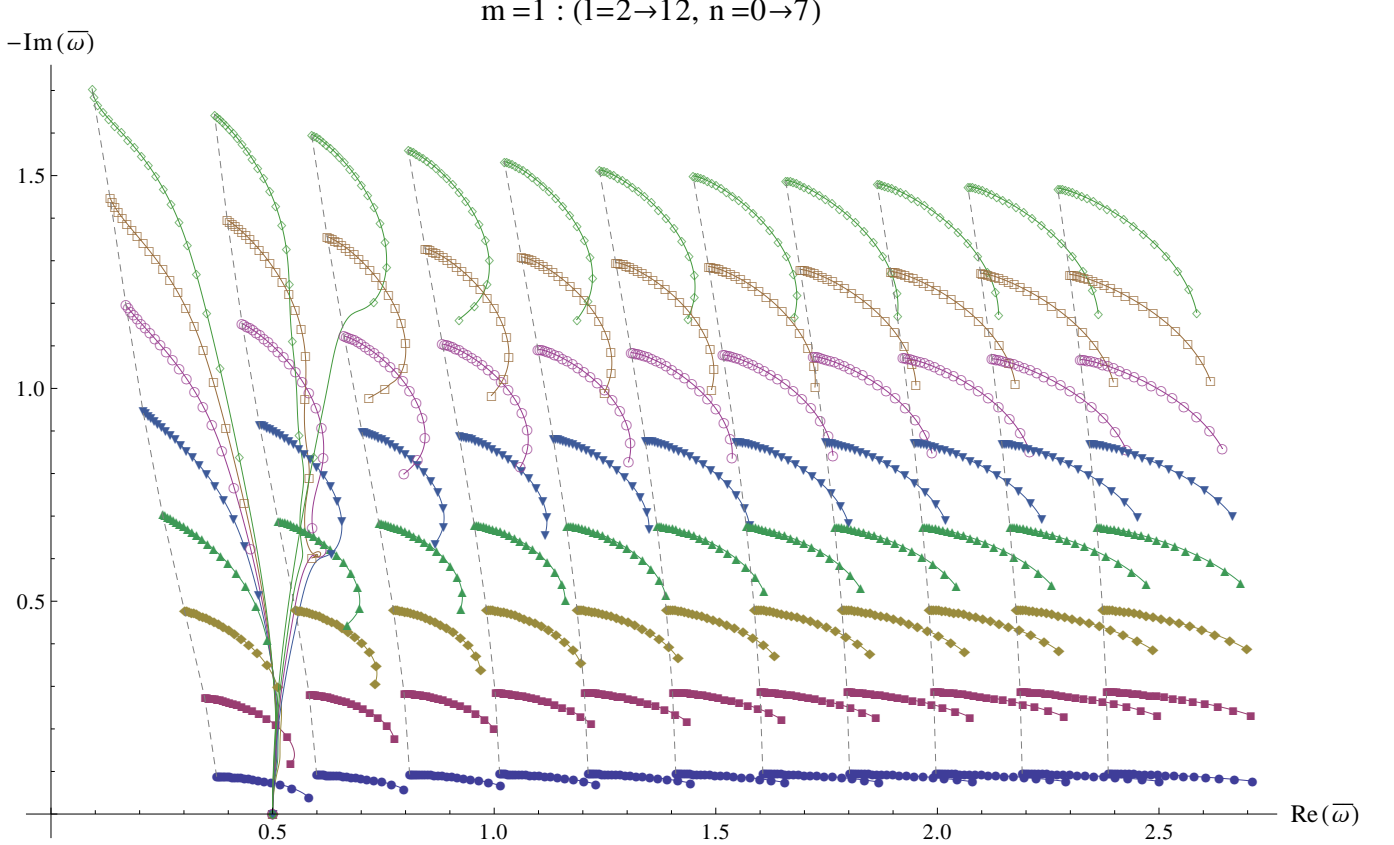
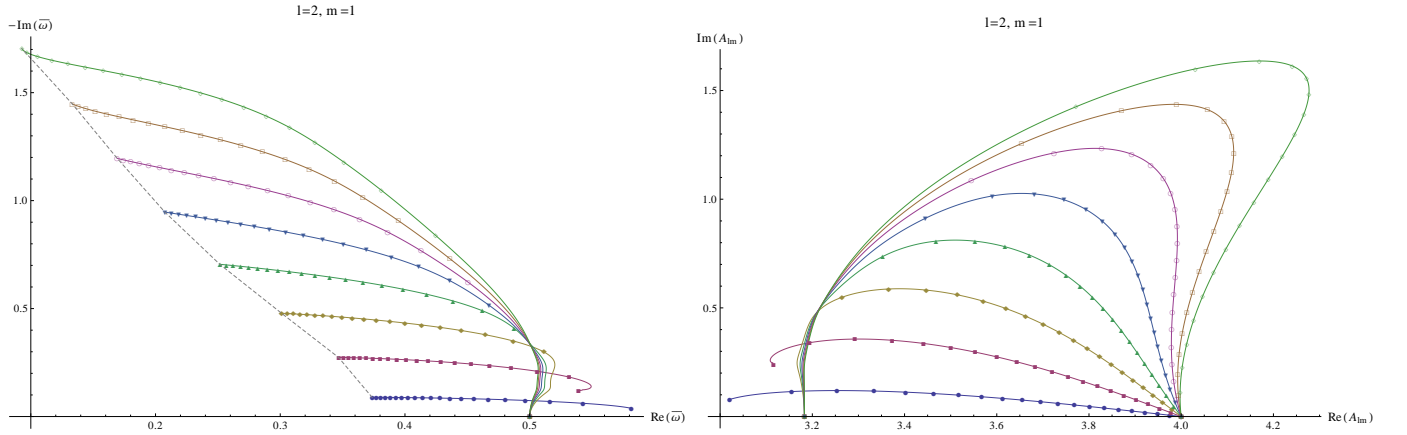
$$\begin{aligned} \text{Re}_{[s]} A_{\ell m} &= \ell(\ell + 1) - s(s + 1) + \beta_1 \\ &\quad + (\beta_2 + \beta_3 \tilde{n} + \beta_4 \tilde{n}^2) \epsilon \end{aligned} \quad (64c)$$

$$\text{Im}_{[s]} A_{\ell m} = \left(\beta_5 + \tilde{n} + \frac{1}{2} \right) \beta_6 \sqrt{\frac{\epsilon}{2}} + (\beta_7 + \beta_8 \tilde{n}) \epsilon \quad (64d)$$

In this case, we see that the coefficient α_3 in Eq. (64b) corresponds to the imaginary part of δ in Eq. (61). The

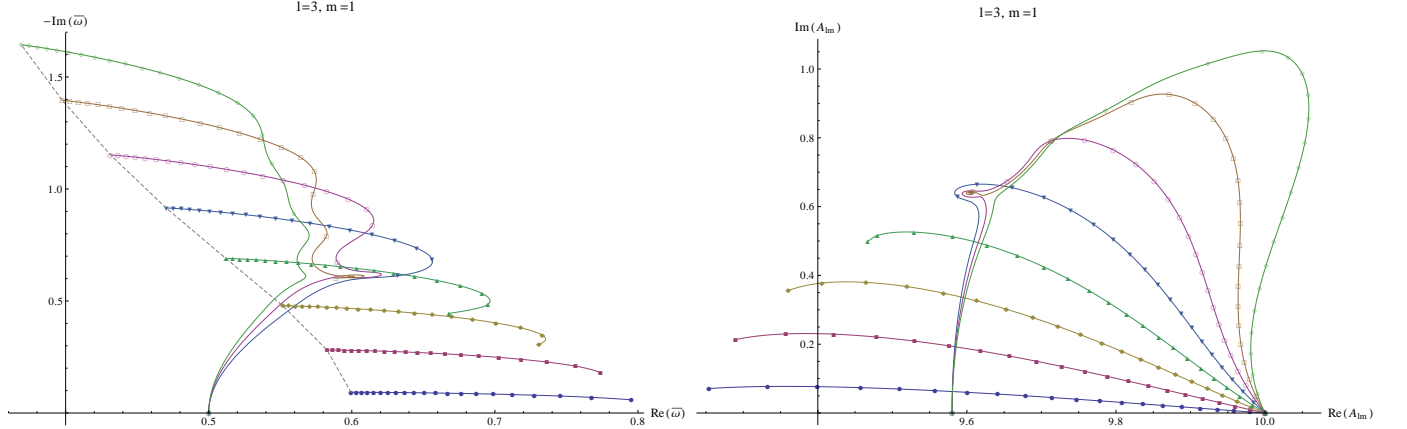
difference between Eqs. (63) and (64) is not simply the switch of δ from real to imaginary. If that were the case, then we should find $\alpha_4 = \alpha_5/2$ in Eq. (64b). The fit values for all cases with $\delta^2 < 0$ are shown in Tables III and IV. We clearly see in Table III that the fit value for α_3 is in excellent agreement with $\text{Im}(\delta)$, and that $\alpha_4 \neq \alpha_5/2$. Note that there are several cases where the fit data for a given (ℓ, m) pair includes only a single overtone. In these cases, the α_2 and α_5 coefficients cannot be determined.

Figures 21 and 22 present the fits for $\ell = 2$ and $m = 1$, for which $\delta^2 < 0$. This example is chosen because it clearly illustrates the necessity of including a quadratic dependence on \tilde{n} in Eq. (64c). The most striking difference we see between Figs. 21 and 19 is the strong dependence on the overtone index \tilde{n} in the $\text{Re}(\bar{\omega})$. What had been the next to leading order behavior for $\delta^2 > 0$ is now the leading order behavior when $\delta^2 < 0$. The same is true for the separation constant. As seen in Eq. (64c), the leading order behavior has a quadratic dependence on \tilde{n} . This is similar to the next to leading order behavior seen in Eq. (63c); however, in this case $\beta_3 \neq \beta_5$. Also, the necessity of the quadratic dependence can be clearly seen in Fig. 22. Finally, as we found for $\delta^2 > 0$,

FIG. 10. Kerr QNM mode sequences for $m = 1$. See Fig. 2 for a full description.FIG. 11. Kerr QNM mode sequences for $\ell = 2$ and $m = 1$. Plots are as described in Fig. 3.

the leading order behavior of $\text{Im}({}_s A_{\ell m})$ is proportional to the leading order behavior of $\text{Im}(\bar{\omega})$. We see this from the fact that, in Table IV, the fitting coefficient β_5 is in excellent agreement with $\text{Im}(\delta)$. Recalling from above that a small set of the fits were made with only a single overtone, we note that in these cases we cannot determine β_3 and β_4 . Furthermore, we cannot separately fit for both β_5 and β_6 . In these cases we have fixed $\beta_5 = \text{Im}\delta$ and fit only for β_6 . The fit values for β_5 and β_6 are marked

with an asterisk when this modified fitting has been used. There were also two cases where only two overtones were available for fits. For these cases, β_3 and β_4 cannot be distinguished and these fit values are also marked with an asterisk.

FIG. 12. Kerr QNM mode sequences for $\ell = 3$ and $m = 1$. Plots are as described in Fig. 3.

ℓ	m	δ_r	α_1	α_2	α_3	α_4
2	2	2.05093	2.05084(3)	1.64(6)	-0.032(8)	1.343(5)
3	3	2.79361	2.79361	2.289(2)	-0.0004(1)	1.35730(9)
4	4	3.56478	3.56478	2.79572(9)	-0.00020(1)	1.34522(2)
5	4	1.07271	1.0687(9)	-28.(2)	-3.4(3)	-17.90(6)
5	5	4.35761	4.35761	3.29989(7)	-0.000142(8)	1.33085(2)
6	5	2.37521	2.37515(1)	-5.50(3)	-0.672(3)	-1.206(1)
6	6	5.16594	5.16594	3.81003(7)	-0.000111(8)	1.31809(2)
7	6	3.40439	3.40438	-2.03(4)	-0.0109(4)	0.2931(3)
7	7	5.98547	5.98547	4.32747(7)	-0.000091(8)	1.30757(2)
8	7	4.35924	4.35924	-0.274(1)	-0.0034(1)	0.74198(9)
8	8	6.81327	6.81327	4.85207(7)	-0.000078(8)	1.29905(2)
9	8	5.28081	5.28081	0.9429(5)	-0.00150(6)	0.93670(4)
10	8	2.80128	2.80099(6)	-22.9(1)	-0.43(2)	-6.456(9)
9	9	7.64735	7.64734	5.38314(7)	-0.000069(8)	1.29217(2)
10	9	6.18436	6.18436	1.92226(3)	-0.000080(3)	1.03870(2)
11	9	4.05104	4.05101	-11.00(2)	-0.053(2)	-1.568(1)
10	10	8.48628	8.48628	5.91988(8)	-0.000062(9)	1.28657(2)
11	10	7.07706	7.07706	2.7754(2)	-0.00048(2)	1.09871(1)
12	10	5.14457	5.14457(1)	-6.269(5)	-0.0147(6)	-0.2362(5)
11	11	9.32904	9.32904	6.46155(8)	-0.000056(9)	1.28198(2)
12	11	7.96274	7.96274	3.5535(1)	-0.00032(1)	1.13691
12	12	10.1749	10.1749	7.00748(8)	-0.00005(1)	1.27819(2)

TABLE I. Values for the coefficients of the fitting function for $\bar{\omega}$ given in Eqs. (63a) and (63b) appropriate for $\delta^2 > 0$. $\delta = \delta_r$ obtained from Eq. (62). All quantities are displayed to six significant digits unless the fit yielded fewer significant digits. In this case, each result is shown to its last significant digit along with its one-sigma error in this last digit printed in parentheses.

2. Zero-frequency modes

Another interesting regime for QNMs occurs when modes approach the negative imaginary axis. These modes seem to share a connection with the “algebraically special” modes[20, 36, 37], sometimes referred to as TTM_Ls. These will be discussed in some detail in Sec. III B. The most easily accessible examples of such behavior is found in the various $n = 8$ overtones of $\ell = 2$. As $\bar{a} \rightarrow 0$, we find that these modes approach the negative imaginary axis and, in fact, appear to approach the frequency of the algebraically special mode of Schwarzschild[5, 8] at $\bar{\omega} = -2i$. There has been some controversy as to whether such QNMs can actually ex-

ist with zero frequency (see the introduction of Ref. [22] and Appendix A of Ref. [1] for additional details, and Sec. III B 1 below for additional discussion). In a very detailed treatment, Maassen van den Brink[22] claims that, for the Zerilli equation, the algebraically special modes are simultaneously a QNM and a TTM_L. Furthermore, he shows that a set of standard Kerr QNMs branch from each of these algebraically special modes. For the case of $\ell = 2$ he finds (translated to our notation)

$$\bar{\omega}_{2m8}(\bar{a}) = -2i - \frac{8269544}{700009}m\bar{a} + \frac{436576}{41177}i\bar{a}^2 + O(m\bar{a}^2) + O(\bar{a}^4). \quad (65)$$

ℓ	m	β_1	β_2	β_3	β_4	β_5	β_6	β_7
2	2	-3.45631	8.8067(4)	-3.6(5)	0.2(1)	0.50(2)	4.29457(3)	-7.81(7)
3	3	-4.30428	10.7854	-5.82(1)	0.367(2)	0.3700(3)	3.86073	-7.304(1)
4	4	-4.95763	12.6174	-6.741(2)	0.3135(3)	0.31347(5)	3.53946	-6.9957(1)
5	4	-3.40071	2.4883(6)	106.(8)	-4.(2)	1.9(2)	2.3473(2)	40.6(5)
5	5	-5.48880	14.3063	-7.692(2)	0.2692(3)	0.26919(4)	3.28306	-6.7150(1)
6	5	-4.14163	5.65809(8)	18.6(1)	0.16(2)	0.174(3)	2.38233	2.072(5)
6	6	-5.93698	15.8614	-8.689(1)	0.2338(3)	0.23376(4)	3.07037	-6.4620(1)
7	6	-4.83985	8.18217(1)	10.53(1)	0.143(3)	0.1425(3)	2.40344	-1.6728(7)
7	7	-6.32583	17.2963	-9.707(1)	0.2050(3)	0.20498(4)	2.88971	-6.2322(1)
8	7	-5.50298	10.5277	6.694(4)	0.1298(7)	0.1298(1)	2.41504	-2.9234(3)
8	8	-6.67066	18.6259	-10.724(1)	0.1812(2)	0.18128(3)	2.73376	-6.0215(1)
9	8	-6.13691	12.7798	4.067(1)	0.1204(3)	0.12043(4)	2.42005	-3.5389(1)
10	8	-6.09714	6.8962(4)	67.3(5)	0.3(1)	0.25(1)	2.46263(1)	14.63(3)
9	9	-6.98190	19.8640	-11.727(1)	0.1615(2)	0.16153(3)	2.59750	-5.8270(1)
10	9	-6.74626	14.9684	1.9491(5)	0.1126(1)	0.11262(1)	2.42037	-3.90733(6)
11	9	-6.91089	10.2630	37.66(7)	0.13(1)	0.127(2)	2.53351	2.964(4)
10	10	-7.26689	21.0230	-12.705(1)	0.1449(2)	0.14490(3)	2.47729	-5.6465(1)
11	10	-7.33472	17.1075	0.0864(2)	0.10586(5)	0.105861(6)	2.41732	-4.15457(2)
12	10	-7.71665	13.3413	26.46(2)	0.111(4)	0.1110(5)	2.59329	-0.522(2)
11	11	-7.53100	22.1136	-13.6557(9)	0.1308(2)	0.13076(3)	2.37041	-5.4786(1)
12	11	-7.90526	19.2047	-1.6321(3)	0.09987(5)	0.099874(7)	2.41182	-4.33282(1)
12	12	-7.77823	23.1451	-14.5753(9)	0.1186(2)	0.11864(2)	2.27472	-5.32201(9)

TABLE II. Values for the coefficients of the fitting function for ${}_{-2}A_{\ell m}(\bar{a}\bar{\omega})$ given in Eqs. (63c) and (63d) appropriate for $\delta^2 > 0$. See Table I for additional details.

ℓ	m	δ_i	α_1	α_2	α_3	α_4	α_5
2	1	1.91907	3.23813(3)	1.54514(1)	1.91906	-0.021(3)	-0.0109(4)
3	1	3.17492	2.11224	0.710824(1)	3.17492	-0.0061(4)	-0.0022(1)
4	1	4.26749	1.82009	—	4.26749	-0.0048(3)	—
3	2	1.87115	7.2471(9)	3.4744(2)	1.87108(1)	-0.12(2)	-0.061(2)
4	2	3.47950	4.19465(1)	1.30534	3.47950	-0.0106(8)	-0.0040(2)
5	2	4.72816	3.61332	0.882398(1)	4.72816	-0.0067(3)	-0.0018(2)
4	3	1.37578	22.66(2)	12.807(4)	1.37549(4)	-1.6(3)	-0.87(4)
5	3	3.54313	6.80319(2)	2.05358(1)	3.54312	-0.024(2)	-0.0094(4)
6	3	4.98492	5.59000	1.29263	4.98492	-0.0103(6)	-0.0029(2)
7	3	6.24553	5.13084	—	6.24552	-0.0077(4)	—
6	4	3.38736	10.6913(1)	3.26423(5)	3.38733(1)	-0.075(7)	-0.029(1)
7	4	5.07533	7.93057(1)	1.78114(1)	5.07532	-0.018(1)	-0.0053(3)
8	4	6.47378	7.07896	—	6.47378	-0.0100(5)	—
7	5	2.98127	18.146(2)	5.9243(6)	2.98114(1)	-0.32(3)	-0.131(5)
8	5	5.01168	10.9114	2.43320(1)	5.01167	-0.033(2)	-0.0101(5)
9	5	6.57480	9.30775	1.66898(1)	6.57480	-0.0152(7)	-0.0036(4)
8	6	2.19168	43.25(9)	16.68(2)	2.1906(1)	-2.9(3)	-1.45(3)
9	6	4.78975	15.0733(1)	3.41635(4)	4.78972	-0.077(6)	-0.024(1)
10	6	6.55627	11.9630	2.12050(1)	6.55626	-0.0252(1)	-0.0063(4)
11	6	8.06162	10.7711	—	8.06162	-0.0153(8)	—
10	7	4.38687	21.7120(5)	5.1575(2)	4.38680(1)	-0.21(2)	-0.068(3)
11	7	6.41836	15.2830	2.71488(1)	6.41835	-0.042(2)	-0.0108(7)
12	7	8.07005	13.2593	—	8.07005	-0.021(1)	—
11	8	3.74604	34.980(6)	9.159(2)	3.74569(3)	-0.91(8)	-0.32(1)
12	8	6.15394	19.6999(1)	3.56155(4)	6.15392	-0.084(5)	-0.022(1)
12	9	2.70389	79.21(6)	25.64(2)	2.7015(3)	-7.2(8)	-3.20(7)

TABLE III. Values for the coefficients of the fitting function for $\bar{\omega}$ given in Eqs. (64a) and (64b) appropriate for $\delta^2 < 0$. $\delta = i\delta_i$ obtained from Eq. (62). See Table I for additional details.

ℓ	m	δ_i	β_1	β_2	β_3	β_4	β_5	β_6	β_7	β_8
2	1	1.91907	-0.817168	-3.41373(8)	-1.42243(6)	0.32846(1)	1.91908(1)	1.94872	0.000(7)	0.044(2)
3	1	3.17492	-0.419864	0.636795(1)	0.514828(1)	0.167730(1)	3.17493	1.01001	0.0046(5)	0.0053(4)
4	1	4.26749	-0.288496	2.86068	—	—	4.26749*	0.750315*	0.0043(2)	—
3	2	1.87115	-1.74881	-12.322(2)	-6.493(1)	0.2325(2)	1.87121(2)	2.18260	-0.05(5)	0.25(1)
4	2	3.47950	-1.14307	-2.24180	-0.685669(7)	0.154790(2)	3.47951	1.46904	0.010(2)	0.01341(9)
5	2	4.72816	-0.894475	1.27953	0.400252*	0.400252*	4.72817	1.24091	0.0091(6)	0.0062(9)
4	3	1.37578	-2.60722	-47.50(4)	-28.71(3)	0.215(4)	1.37604(7)	2.28731(3)	-1.3(8)	3.7(2)
5	3	3.54313	-1.94623	-6.97433(4)	-2.44406(4)	0.146252(9)	3.54315(1)	1.76588	0.019(5)	0.034(2)
6	3	4.98492	-1.65057	-1.78614(1)	-0.332540(8)	0.158689(4)	4.98493	1.60394	0.0158(1)	0.012(1)
7	3	6.24553	-1.49341	2.43042(1)	—	—	6.24553*	1.54481*	0.0157(9)	—
6	4	3.38736	-2.77576	-15.1115(3)	-5.3855(3)	0.13901(5)	3.38741(1)	1.98024	0.04(2)	0.111(6)
7	4	5.07533	-2.49104	-6.48399(1)	-1.67232(2)	0.151562(5)	5.07534	1.88766	0.027(3)	0.023(2)
8	4	6.47378	-2.34013	-1.30084(1)	—	—	6.47378*	1.87150*	0.024(1)	—
7	5	2.98127	-3.61202	-31.920(4)	-11.791(3)	0.1344(6)	2.98143(3)	2.14367(1)	0.15(8)	0.51(3)
8	5	5.01168	-3.38311	-13.4092(1)	-3.55546(5)	0.14478(2)	5.01169	2.11696	0.051(6)	0.045(3)
9	5	6.57480	-3.27195	-6.54422(1)	-0.570367(2)*	-0.570367(2)*	6.57481(1)	2.14543(1)	0.037(2)	0.019(3)
8	6	2.19168	-4.44655	-88.9(2)	-38.1(1)	0.28(2)	2.1924(3)	2.2721(1)	1.(1)	5.1(3)
9	6	4.78975	-4.30830	-23.9745(2)	-6.4163(2)	0.13857(5)	4.78979(1)	2.30668	0.10(2)	0.109(6)
10	6	6.55627	-4.26538	-13.6545	-2.87125(4)	0.15400(2)	6.55628(1)	2.37885	0.059(4)	0.033(3)
11	6	8.06162	-4.26020	-6.76295(1)	—	—	8.06162*	2.45322*	0.049(3)	—
10	7	4.38687	-5.25539	-41.747(1)	-11.427(1)	0.1334(3)	4.38697(2)	2.46644(1)	0.26(4)	0.31(2)
11	7	6.41836	-5.30470	-23.3442(1)	-4.9645(1)	0.14755(5)	6.41838(1)	2.58040	0.100(8)	0.058(6)
12	7	8.07005	-5.37425	-14.4186	—	—	8.07005*	2.68892*	0.071(4)	—
11	8	3.74604	-6.21720	-78.26(2)	-22.80(1)	0.136(3)	3.74647(9)	2.60270(3)	0.8(2)	1.48(7)
12	8	6.15394	-6.37897	-37.0045(2)	-7.9329(3)	0.14171(8)	6.15399(1)	2.75634	0.18(2)	0.120(9)
12	9	2.70389	-7.18896	-200.7(2)	-69.3(1)	0.18(2)	2.7059(7)	2.7190(3)	4.(3)	13.9(8)

TABLE IV. Values for the coefficients of the fitting function for ${}_{-2}A_{\ell m}(\bar{a}\bar{\omega})$ given in Eqs. (64c) and (64d) appropriate for $\delta^2 < 0$. $\delta = i\delta_i$ obtained from Eq. (62). Special situations where results are marked with an asterisk(*) are discussed in the text. See Table I for additional details.

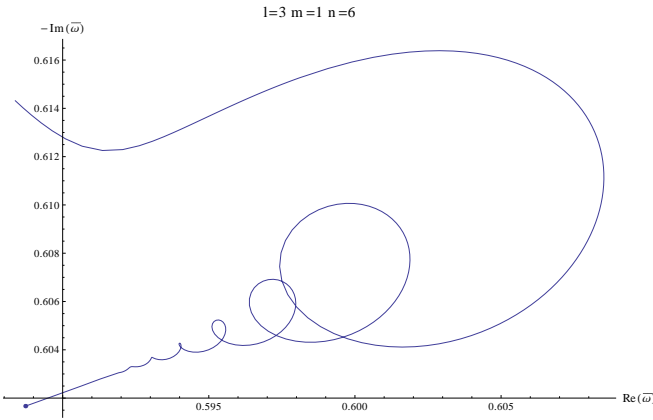


FIG. 13. Close-up of $\bar{\omega}$ for the $\{3, 1, 6\}$ sequence showing the unusual termination of this sequence. See Fig. 12 for context.

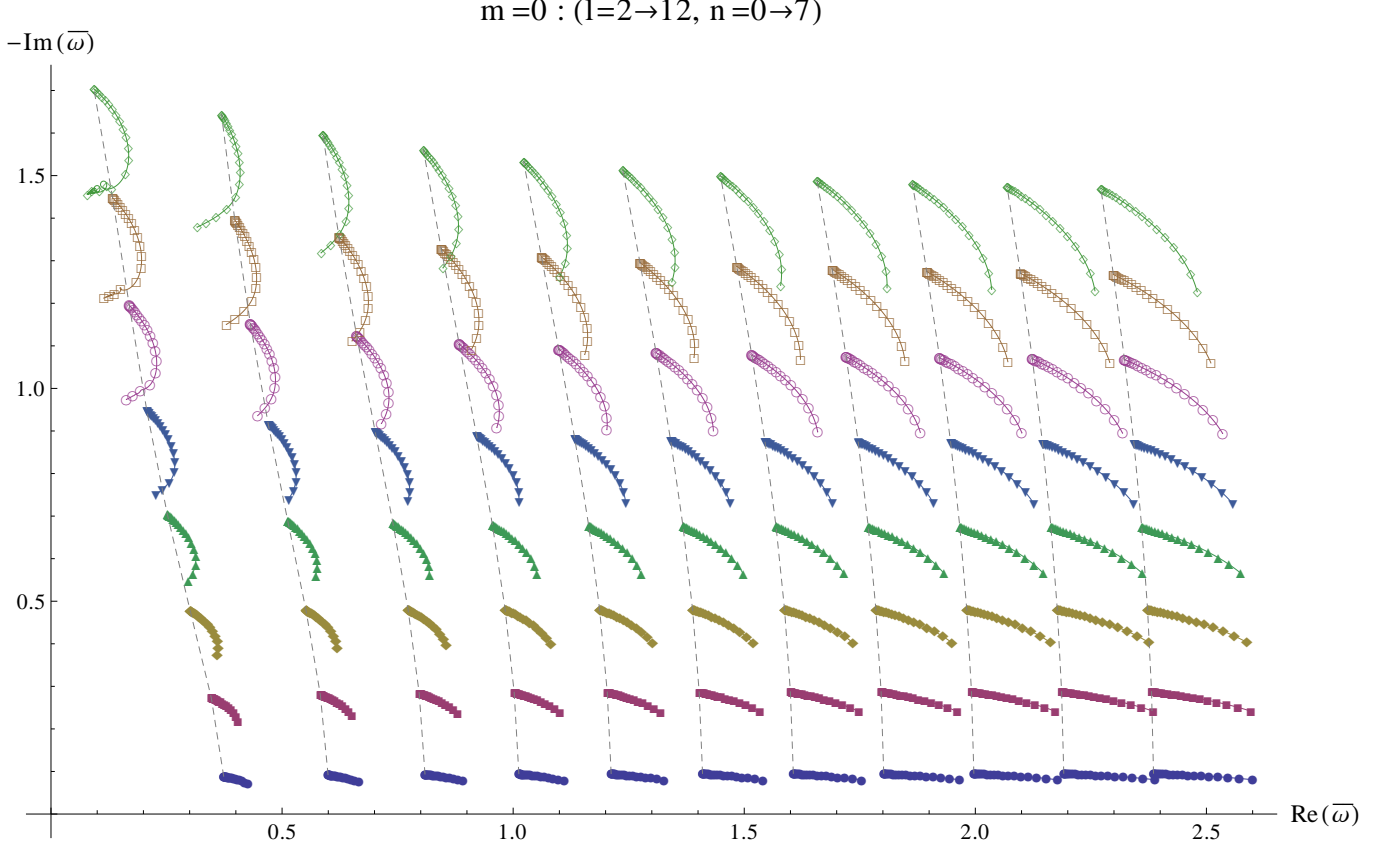
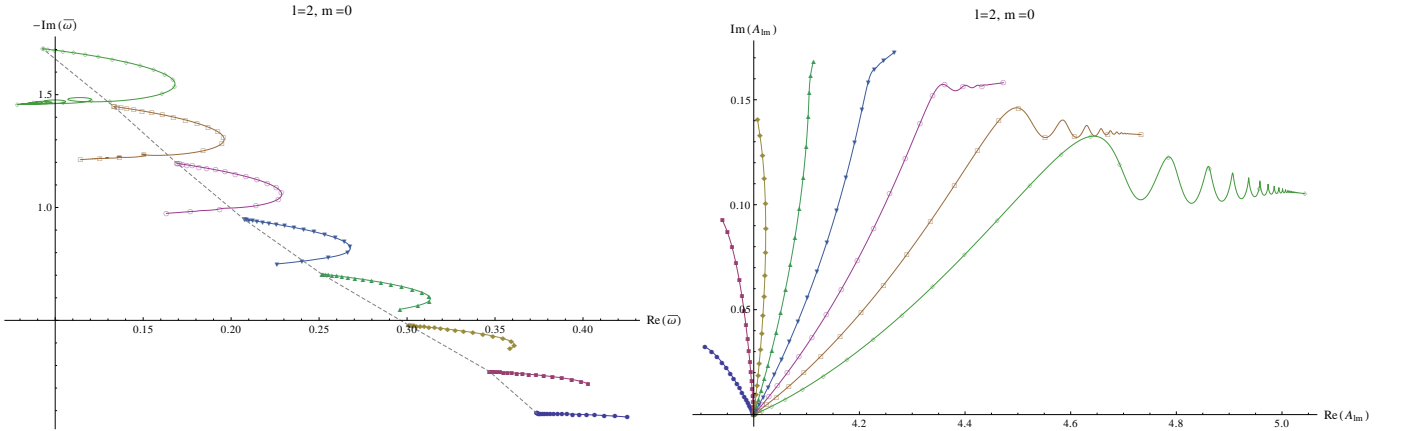
For positive-frequency modes, Eq. (65) only applies to $m \leq 0$. For the cases with $m > 0$, Maassen van den Brink[22] suggested several possible behaviors, and in a later paper[38] he and coauthors suggested that the $m > 0$ modes might be related to a pair of “unconventional damped modes” that seem to exist on the unphysical sheet lying behind a branch cut. Of this pair, one set of modes is associated with the positive-frequency modes and the other with the negative-frequency modes. The

unconventional QNMs were predicted to be at

$$\bar{\omega}_{\pm} = \mp 0.013 + (0.0016 - 2)i, \quad (66)$$

with $\bar{\omega}_+$ serving as the $\bar{a} \rightarrow 0$ limit for the positive-frequency $m = 1$ and 2 modes. The authors suggest that the modes will move through the NIA as \bar{a} is tuned.

To our knowledge, the best numerical results to date[8, 28] have not followed these sequences to very small values of \bar{a} except perhaps for the $m = 0$ case. It is, in fact, quite challenging to obtain solutions close to the imaginary axis. Using the methods described in Secs. II C and II D we have obtained solutions down to $\bar{a} = 10^{-6}$ for $m \in \{0, -1, -2\}$. The right plot in Fig. 23 shows our results for $\bar{\omega}$. While we have not been able to find solutions for these modes for $\bar{a} = 0$, our results are consistent with these modes beginning at $\bar{a} = 0$ at $\bar{\omega} = -2i$. For both $m = 1$ and 2 , we find a *pair of solutions* associated with $n = 8$. This was first seen in Ref. [28] (see the left panel of their Fig. 10). The left plot in Fig. 23 shows both pairs of solutions including their approach to the accumulation points at $\bar{\omega} = m/2$. We refer to these multiple solutions as ‘overtone multiplets’ and distinguish them via a subscript on the overtone. The use of multiplets is appropriate as confirmed by the behavior of these modes near the accumulation points. For both the $m = 1$ and 2 cases, the $n = 8_0$ and 8_1 mode sequences approach the accumulation points at $\bar{\omega} = m/2$ between the sequences

FIG. 14. Kerr QNM mode sequences for $m = 0$. See Fig. 2 for a full description.FIG. 15. Kerr QNM mode sequences for $\ell = 2$ and $m = 0$. Plots are as described in Fig. 3.

that extend from the $n = 7$ and $n = 9$ (not shown in this paper) Schwarzschild QNMs. Interestingly, these mode sequences do not seem to start at $\bar{a} = 0$. Instead, they begin at the NIA at a finite value for \bar{a} . Table V lists the starting values for $\bar{\omega}$ and \bar{a} for each of these overtone multiplets.

We have obtained $\bar{a} \rightarrow 0$ fits of our numerical results

Mode	$\bar{\omega}$	\bar{a}
{2, 2, 80}	$-1.96384i$	0.0034826
{2, 1, 80}	$-1.96407i$	0.0068819
{2, 2, 81}	$-2.04223i$	0.0053279
{2, 1, 81}	$-2.04259i$	0.0108327

TABLE V. Initial values for $\bar{\omega}$ and \bar{a} for the $\ell = 2$ multiplets of $m = 1$ and 2 . The “first” multiplet is labeled by $n = 80$ and the “second” by $n = 81$.

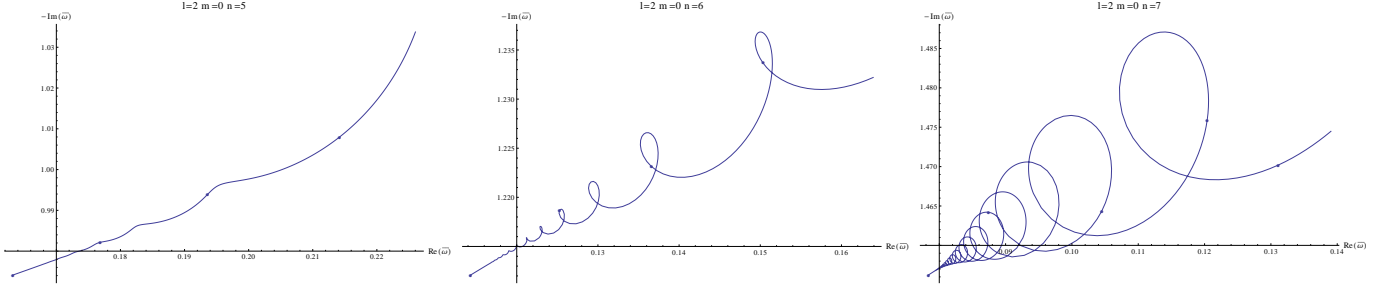


FIG. 16. Close-up of $\bar{\omega}$ for the $\{2, 0, 5-7\}$ sequence showing the unusual termination of these sequences. See Fig. 15 for context.

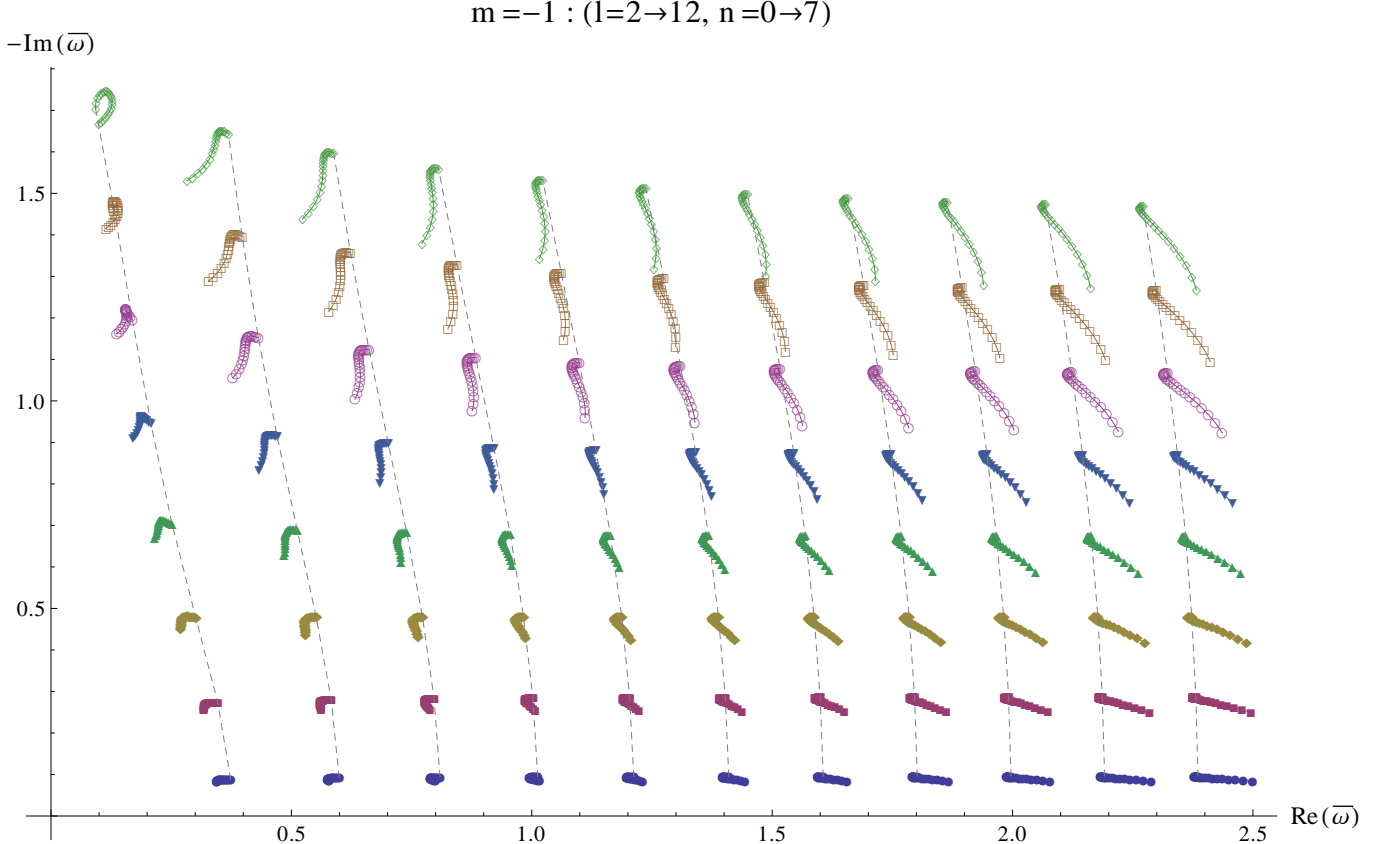


FIG. 17. Kerr QNM mode sequences for $m = -1$. See Fig. 2 for a full description.

for the $\{2, m, 8\}$ mode sequences. The results are

$$\bar{\omega}_{2-28}(\bar{a}) = -2i + 23.29(4)\bar{a} - 4220(15)i\bar{a}^2, \quad (67a)$$

$$\bar{\omega}_{2-18}(\bar{a}) = -2i + 11.70(1)\bar{a} - 1080(2)i\bar{a}^2, \quad (67b)$$

$$\bar{\omega}_{208}(\bar{a}) = -2i + 10.60i\bar{a}^2 + 7781\bar{a}^4, \quad (67c)$$

$$\begin{aligned} \bar{\omega}_{218_0}(\bar{a}) = & -0.007323 + 1.235\bar{a} - 2.065\bar{a}^{3/2}, \\ & -1.989i + 5.554i\bar{a} - 24.00i\bar{a}^{3/2}, \end{aligned} \quad (67d)$$

$$\begin{aligned} \bar{\omega}_{218_1}(\bar{a}) = & -0.008364 + 0.7306\bar{a} + 0.3983(1)\bar{a}^{3/2} \\ & -2.013i - 4.367i\bar{a} + 15.91i\bar{a}^{3/2}, \end{aligned} \quad (67e)$$

$$\begin{aligned} \bar{\omega}_{228_0}(\bar{a}) = & -0.007315 + 2.460\bar{a} - 6.096\bar{a}^{3/2} \\ & -1.989i + 11.02i\bar{a} - 66.83i\bar{a}^{3/2}, \end{aligned} \quad (67f)$$

$$\begin{aligned} \bar{\omega}_{228_1}(\bar{a}) = & -0.008375 + 1.476\bar{a} + 1.312(2)\bar{a}^{3/2} \\ & -2.013i - 8.797(2)i\bar{a} + 45.70(2)i\bar{a}^{3/2}, \end{aligned} \quad (67g)$$

where we display results to four significant digits unless the fit yielded fewer. In that case, we also display in parentheses the one-sigma uncertainty in the fit.

In Ref. [28], the authors compare their numerical results to the predictions of Maassen van den Brink[22, 38]. They found that “none of the QNMs we numerically found seem to agree with the analytic prediction when the rotation rate a is small,” referring to the prediction of Eq. (65). Their nonagreement is likely due to not having data for sufficiently small \bar{a} . We find that Eqs. (67a), (67b), and (67c) show excellent agreement with Eq. (65). The coefficients for the terms that are linear in \bar{a} are in good agreement with $m \times 8269544/700009$. The imag-

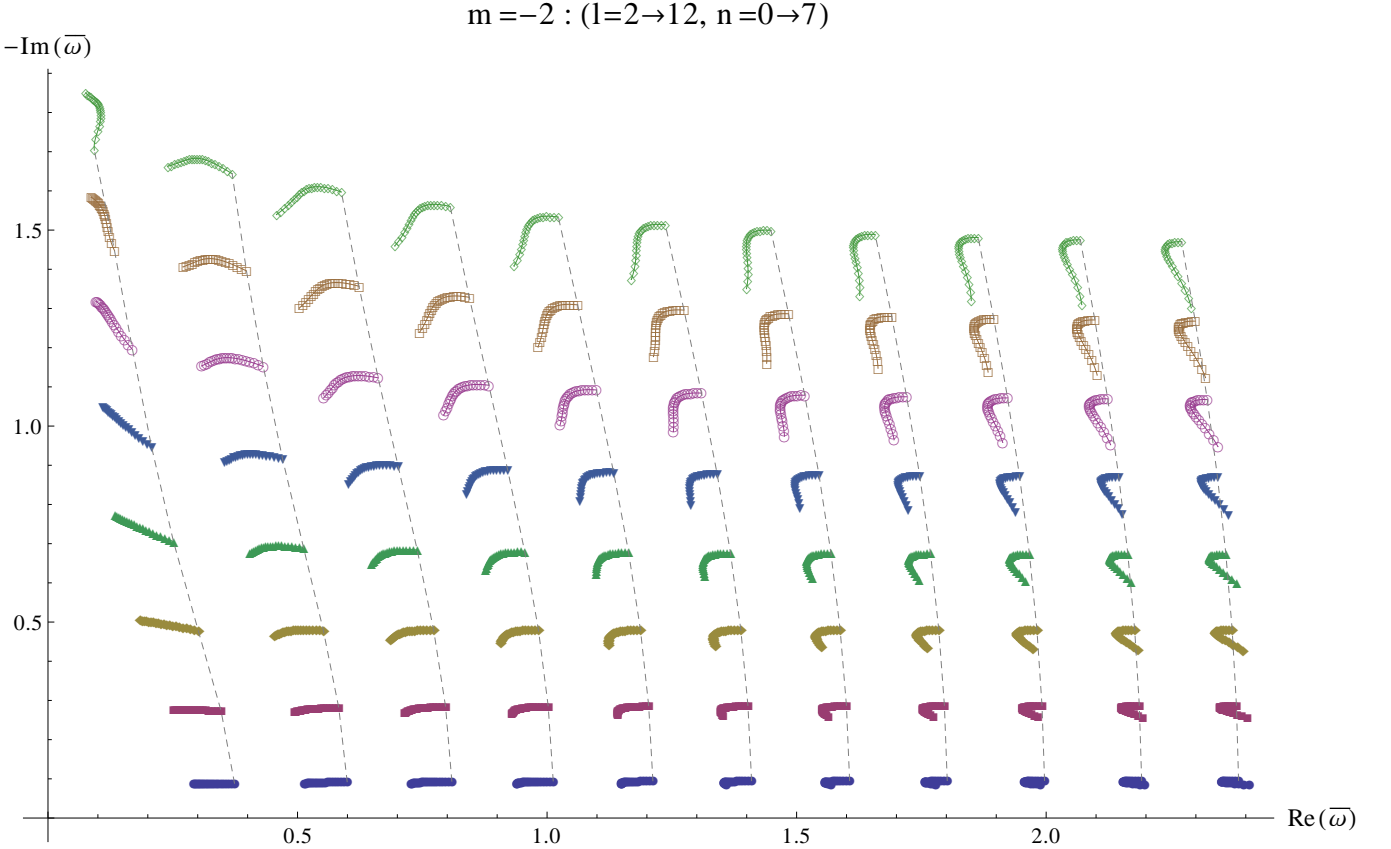


FIG. 18. Kerr QNM mode sequences for $m = -2$. See Fig. 2 for a full description.

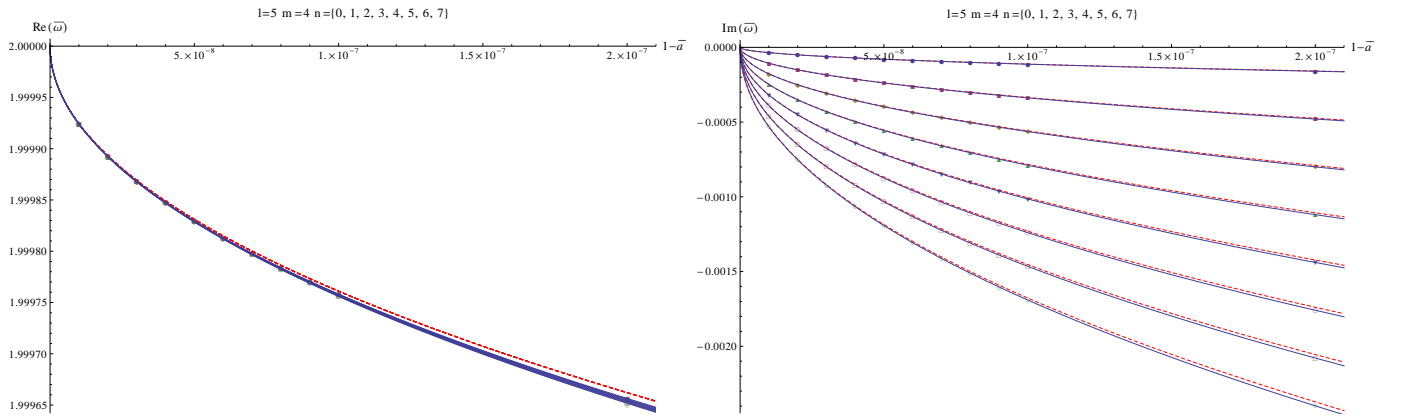


FIG. 19. Near extremal behavior of $\bar{\omega}$ for $\ell = 5$, $m = 4$. Symbols in the left plot represent data values used to fit the coefficients in Eq. (63a). The lines represent the resulting fit function. The right plot corresponds to Eq. (63b). In both plots, the dashed(red) line represents the fit function omitting the next to leading order behavior in ϵ .

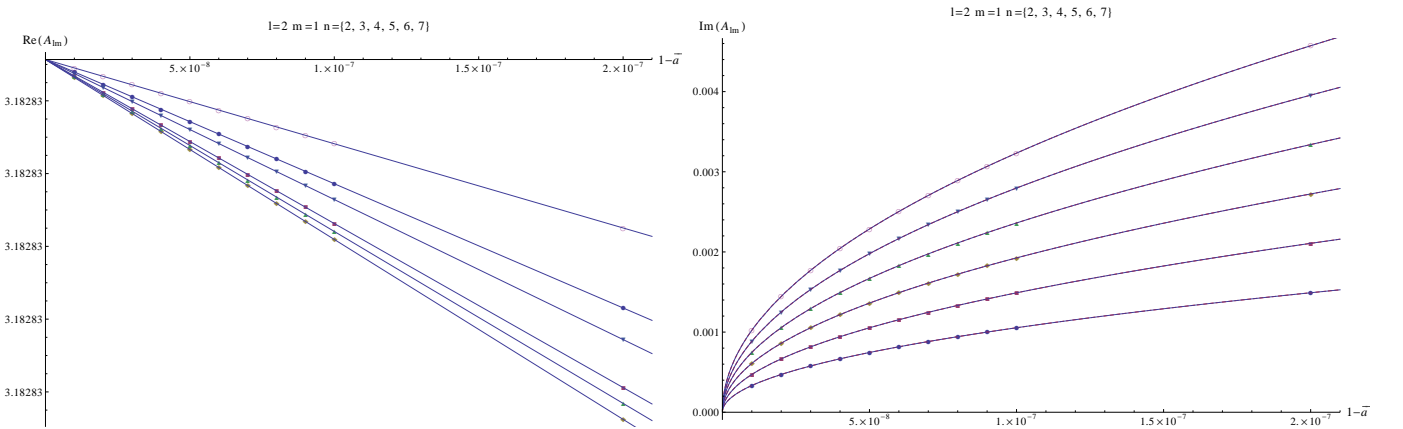
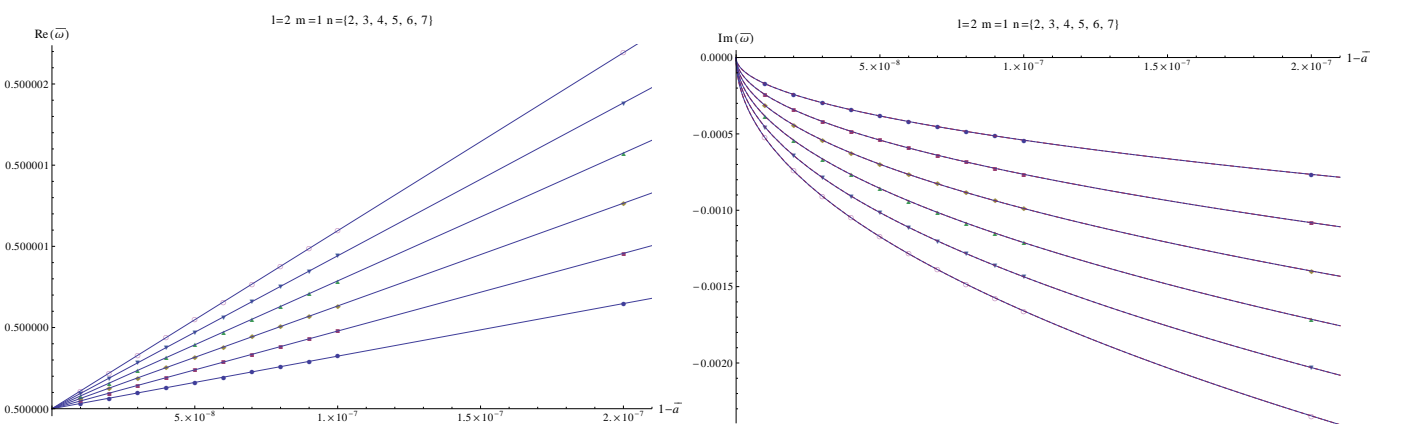
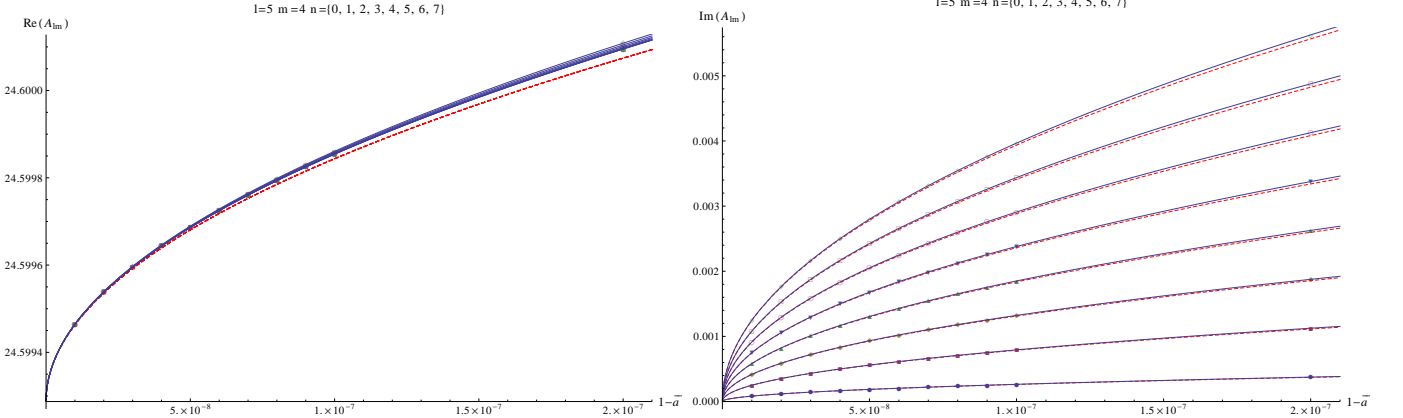
inary term that is quadratic in \bar{a} in Eq. (67c) is in good agreement with $436576/41177$. Coefficients for the higher-order terms in these three equations are not determined in Eq. (65), but are of the prescribed form. Interestingly, while Eq. (65) predicts that $\bar{\omega}_{2-28}(\bar{a}) = \bar{\omega}_{2-18}(2\bar{a})$ up to linear order, we find that it is a good approximation including the quadratic term in \bar{a} .

Our results for the $m = 1$ and 2 multiplets seem to fol-

low the general predictions of Ref. [38], except that the multiplets suggest that there are *two* pairs of unconventional modes in the Schwarzschild limit, not the single pair they found. The first, associated with Eqs. (67d) and (67f) extrapolates to

$$\bar{\omega} \approx -0.0073 + (0.011 - 2)i, \quad (68)$$

while the second, associated with Eqs. (67e) and (67g)



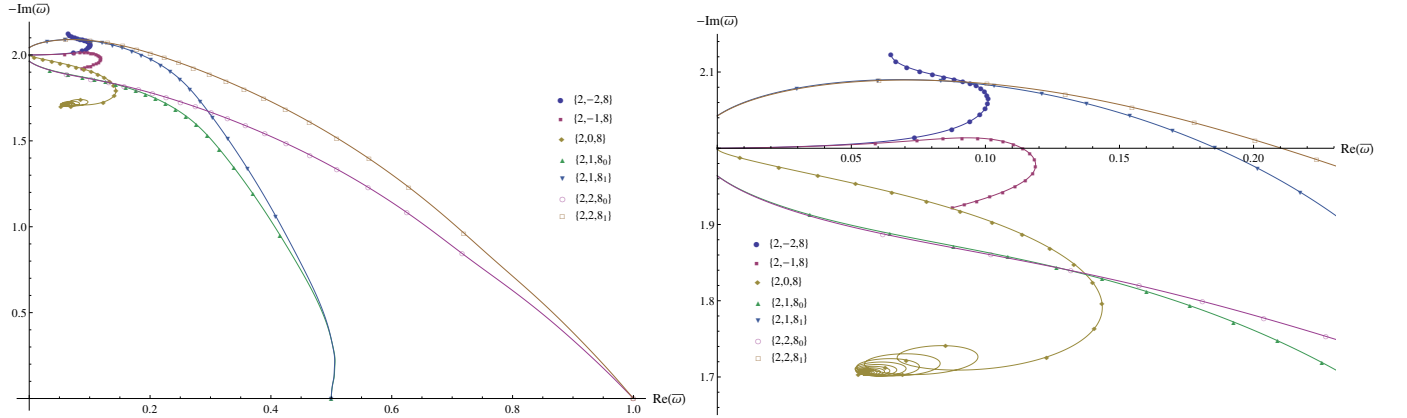


FIG. 23. Behavior of $\bar{\omega}$ for all $n = 8$ overtones of $\ell = 2$. The left plot shows the full extent of all sequences with $-2 \leq m \leq 2$ and clearly shows that the $m = 1$ and $m = 2$ modes are both multiplets. The multiplets are distinguished by a subscript on the overtone index. The right plot shows a close-up of the behavior near the NIA. Note that the $m = 1, 2$ modes for the $n = 8_0$ multiplet approach the NIA near $\bar{\omega} = -1.964$ while the modes for the $n = 8_1$ multiplet approach the NIA near $\bar{\omega} = -2.042$.

extrapolates to

$$\bar{\omega} \approx -0.0084 + (-0.013 - 2)i. \quad (69)$$

Again, our results for $m = 1$ and 2 are significantly different from the related extrapolated results in Ref. [28]. Interestingly, we also find that, to a good approximation, $\bar{\omega}_{228_{0,1}}(\bar{a}) = \bar{\omega}_{218_{0,1}}(2\bar{a})$ for $\bar{a} \rightarrow 0$.

B. Polynomial solutions of the Teukolsky equation

In Sec. II B 3 we described briefly the construction of confluent Heun polynomials. As a concrete example, consider the case of the TTM modes. It is customary to refer to modes which travel away from the black-hole horizon and out at infinity as TTM_L modes, and those traveling into the black-hole horizon and in from infinity as TTM_R modes. These were studied in detail first by Chandrasekhar[20], and later by Andersson[21] and Maassen van den Brink[22]. We will show that these modes can be derived by means of confluent Heun polynomials.

Recall that the radial Teukolsky equation can be put in the form of the confluent Heun equation in eight different ways depending on the choice of the parameters $\{\zeta, \xi, \eta\}$ [see Eqs. (23)]. The parameter ξ affects the behavior of the solution at the black-hole horizon. If we choose $\xi = \xi_+$ then the unphysical solution of modes propagating out of the black hole is represented by the local solution of Eq. (19d), or if we choose $\xi = \xi_-$, then the same unphysical solution is represented by Eq. (19c). Both of these behave at the event horizon like the second form of Eq. (28b). Similarly, ζ_+ and Eq. (19e), or ζ_- and Eq. (19f) both represent modes traveling out at infinity as seen in the first form of Eq. (28c). These two parameters yield four different ways of writing the same physical solutions representing a TTM_L mode. However,

confluent Heun polynomials are simultaneously Frobenius solutions at all three singular points. The choice of η affects the behavior of the solution at the Cauchy horizon and we see that a TTM_L solution can have one of the two different behaviors near the Cauchy horizon given by Eq. (28a).

The two possible solutions with different behaviors at the Cauchy horizon can each be constructed by any of the 4 different decompositions of the radial Teukolsky equation, but they each reduce to the same underlying condition that must be satisfied if a polynomial solution is to exist. That condition, that the second parameter of the local solution [either Eq. (15) or (16)] must be a non-positive integer $-q$, has the following forms for possible TTM_L modes:

$$-q = \begin{cases} \alpha & (\bar{\zeta}_+, \xi_+, \eta_\pm), \\ \alpha + 1 - \delta & (\bar{\zeta}_+, \xi_-, \eta_\pm), \\ -\alpha + \gamma + \delta & (\bar{\zeta}_-, \xi_+, \eta_\pm), \\ \alpha + 1 - \gamma & (\bar{\zeta}_-, \xi_-, \eta_\mp). \end{cases} \quad (70)$$

The combinations of α , γ , and δ are simply the second parameter of the appropriate version of Eqs. (19). In parentheses are the corresponding choices for the parameters $\{\zeta, \xi, \eta\}$. Each line on the right-hand side of Eq. (70) reduces to the same two conditions:

$$q = -1 - 2s \quad \text{or} \quad (71a)$$

$$q = -1 - s - i \frac{2\bar{\omega}(1 - \sqrt{1 - \bar{a}^2}) - \bar{a}m}{\sqrt{1 - \bar{a}^2}}, \quad (71b)$$

depending on the choice of η_\pm . The upper sign choice for η in Eq. (70) corresponds to Eq. (71a) and the lower sign choice to Eq. (71b). The possible solutions with q given by Eq. (71a) correspond to the solution that behaves like $z^{-i\sigma_-}$ at the Cauchy horizon ($z \rightarrow 0$). For q given by Eq. (71b), possible solutions behaves like $z^{-s+i\sigma_-}$ at the Cauchy horizon.

Consider the case where q is given by Eq. (71a). The requirement that q must be a non-negative integer does not fix $\bar{\omega}$, but does require that $s \leq -\frac{1}{2}$ and that s is either an integer or a half integer in magnitude. The requirement on s is sensible given that we require $s \leq 0$ for solutions of the radial Teukolsky equation to represent outgoing waves at infinity. The requirement on s is necessary, but not sufficient to guarantee the existence of polynomial solutions. In conjunction with this condition,

$$\begin{vmatrix} -\sigma_{n3} & 1 - 2i\bar{\omega} + i\frac{2\bar{\omega} - \bar{a}m}{\sqrt{1 - \bar{a}^2}} & 0 & 0 \\ -12i\bar{\omega}\sqrt{1 - \bar{a}^2} & -2 + 4i\bar{\omega}(1 - \sqrt{1 - \bar{a}^2}) - \sigma_{n3} & -4i\bar{\omega} + 2i\frac{2\bar{\omega} - \bar{a}m}{\sqrt{1 - \bar{a}^2}} & 0 \\ 0 & -8i\bar{\omega}\sqrt{1 - \bar{a}^2} & -2 + 8i\bar{\omega}(1 - \sqrt{1 - \bar{a}^2}) - \sigma_{n3} & -3 - 6i\bar{\omega} + 3i\frac{2\bar{\omega} - \bar{a}m}{\sqrt{1 - \bar{a}^2}} \\ 0 & 0 & -4i\bar{\omega}\sqrt{1 - \bar{a}^2} & 12i\bar{\omega}(1 - \sqrt{1 - \bar{a}^2}) - \sigma_{n3} \end{vmatrix} = 0. \quad (72)$$

For the nonspinning case $\bar{a} = 0$, we find the four eigenvalues to be

$$\sigma_{03} = -1 - \sqrt{1 + 12i\bar{\omega}}, \quad (73a)$$

$$\sigma_{13} = -1 - \sqrt{1 - 12i\bar{\omega}}, \quad (73b)$$

$$\sigma_{23} = -1 + \sqrt{1 - 12i\bar{\omega}}, \quad (73c)$$

$$\sigma_{33} = -1 + \sqrt{1 + 12i\bar{\omega}}. \quad (73d)$$

These eigenvalues are associated with Eq. (19a), so we must also compute the corresponding value of σ associated with Eq. (19a). For $\bar{a} = 0$, we find $\sigma = {}_{-2}A_{\ell m}(0) = \ell(\ell + 1) - 2$. Polynomial solutions exist when $\sigma_{nq} = \sigma$. Since $\sigma > 0$, both σ_{03} and σ_{13} are not allowed. Equations. (73c) and (73d) yield

$$\bar{\omega} = \pm \frac{i}{12}(\ell - 1)\ell(\ell + 1)(\ell + 2). \quad (74)$$

σ_{23} has the positive sign and represents an unstable solution. σ_{33} , with the negative sign, represents the physical solution. These frequencies are the well-known algebraically special frequencies of Schwarzschild. Since these appear frequently, we will define them as

$$\bar{\Omega} \equiv -\frac{i}{12}(\ell - 1)\ell(\ell + 1)(\ell + 2). \quad (75)$$

Associated with these frequencies are the confluent Heun polynomial solutions

$$Hc_{33}(i\bar{\Omega}, -1, -1 + 4i\bar{\Omega}; z) = z^2 - \frac{l(l+1)}{3}z^3 \quad (76)$$

which corresponds to the physical solution

$$R(z) = z^2(z - 1)^{2i\bar{\Omega}} \left(1 - \frac{l(l+1)}{3}z\right) e^{2i\bar{\Omega}z}. \quad (77)$$

We note that Eq. (76) does not have the expected behavior for $z \rightarrow 0$. The reason for this is that for $\bar{a} = 0$,

the $\Delta_{q+1} = 0$ condition (see Sec. II B 3) is necessary and sufficient to guarantee the existence of polynomial solutions, and will in fact determine $\bar{\omega}$ when solutions exist.

For gravitational perturbations, $s = -2$ giving $q = 3$. The matrix for the $\Delta_{q+1} = 0$ condition can be constructed from any of the six local solutions in Eqs. (19), but it is easiest to use Eq. (19a). Written as an eigenvalue problem for the quantity σ_{n3} (not to be confused with σ_{\pm}), the determinant of the matrix takes the form

$$\begin{vmatrix} 0 & 0 & 0 & 0 \\ -4i\bar{\omega} + 2i\frac{2\bar{\omega} - \bar{a}m}{\sqrt{1 - \bar{a}^2}} & 0 & 0 & 0 \\ -2 + 8i\bar{\omega}(1 - \sqrt{1 - \bar{a}^2}) - \sigma_{n3} & -3 - 6i\bar{\omega} + 3i\frac{2\bar{\omega} - \bar{a}m}{\sqrt{1 - \bar{a}^2}} & 0 & 0 \\ -4i\bar{\omega}\sqrt{1 - \bar{a}^2} & 12i\bar{\omega}(1 - \sqrt{1 - \bar{a}^2}) - \sigma_{n3} & 0 & 0 \end{vmatrix} = 0. \quad (72)$$

$\gamma = -1$ and the characteristic exponents for the singular point at $z = 0$ (Cauchy horizon) differ by an integer. Only the series solution corresponding to the larger exponent must be in the form of a simple polynomial. The situation is even more interesting, because $\delta = -1 + 4i\bar{\Omega}$ so the characteristic exponents for the singular point at $z = 1$ (event horizon) also differ by an integer. Rewriting Eq. (76) as a local solution at the $z = 1$ regular-singular point, we find that it corresponds to the larger characteristic exponent and the physical solution of Eq. (77) has the desired behavior for a TTM_L mode. However, we will return to further consider the behavior at $z = 1$ below.

Returning to the $\Delta_{q+1} = 0$ condition of Eq. (72), for the general case with $\bar{a} \neq 0$, the corresponding value of σ is

$$\sigma = {}_{-2}A_{\ell m}(\bar{a}\bar{\omega}) + \bar{a}^2\bar{\omega}^2 + \bar{\omega} \left(6i(1 - \sqrt{1 - \bar{a}^2}) - 2\bar{a}m\right). \quad (78)$$

While we could, in principle, follow a similar procedure and equate the eigenvalues for the general case with σ , it is easier to insert this value for σ into the matrix and then simply require that the determinant vanish. The result can be written as

$$0 = \lambda^2(\lambda + 2)^2 + 8\lambda\bar{a}\bar{\omega}(6(\bar{a}\bar{\omega} + m) - 5\lambda(\bar{a}\bar{\omega} - m)) + 144\bar{\omega}^2(1 + \bar{a}^2(\bar{a}\bar{\omega} - m)^2), \quad (79)$$

where

$$\lambda = \lambda_- \equiv {}_{-2}A_{\ell m}(\bar{a}\bar{\omega}) + \bar{a}^2\bar{\omega}^2 - 2m\bar{a}\bar{\omega}, \quad (80)$$

and the right-hand side of Eq. (79) is just the magnitude squared of the Starobinsky constant[20].

We will examine the general solutions associated with Eq. (71a) below, but first, we consider the other possible solution with q given by Eq. (71b). This case is somewhat more complicated. With $s = -2$ we find that, in general, only $q = 0$ can have a stable solution with $\text{Im}(\bar{\omega}) < 0$. The associated matrix is one-dimensional

and trivial, with vanishing eigenvalue. In this case, since $\bar{\omega}$ is fixed, we must find that an eigenvalue equals σ for that frequency in order for a polynomial solution to exist. But in this case, σ is a function of \bar{a} , m , and ${}_2A_{\ell m}(\bar{a}\bar{\omega})$. The $\Delta_{q+1} = 0$ condition is not satisfied and no solution exists for arbitrary \bar{a} . However, if $\bar{a} = 0$, and $s = -2$, we find $q = 1$ for any $\bar{\omega}$, and the $\Delta_{q+1} = 0$ condition leads to the two eigenvalues

$$\sigma_{01} = 1 - \sqrt{1 + 12i\bar{\omega}}, \quad \sigma_{11} = 1 + \sqrt{1 + 12i\bar{\omega}}. \quad (81)$$

With σ_{01} not allowed because it is negative for stable solutions, we find from σ_{11} that $\bar{\omega} = \bar{\Omega}$ again. The associated confluent Heun polynomial solution is

$$Hc_{11}(i\bar{\Omega}, 3, -1 + 4i\bar{\Omega}; z) = 1 - \frac{l(l+1)}{3}z. \quad (82)$$

Interestingly, we find that the corresponding physical solution is identical to Eq. (77) which supposedly has a different boundary condition on the Cauchy horizon. The reason for this is, of course, that the characteristic exponents for the singular point at $z = 0$ (Cauchy horizon) differ by an integer. For $\bar{a} = 0$, the polynomial solutions corresponding to both Eqs. (71a) and (71b) both yield $\bar{\omega} = \bar{\Omega}$ and each is finding the series solution corresponding to the larger characteristic exponent.

Returning to the solutions corresponding to Eq. (71a), when $\bar{a} \neq 0$, $\gamma = -1 - i\sigma_-$ which will not be an integer in general. Therefore a polynomial solution that behaves like $z^{-i\sigma_-}$ at the Cauchy horizon will exist for the TTM_L case when $a \neq 0$. These solutions are the well-known algebraically special solutions which have been studied in the past. The associated polynomial solution is a simple cubic function of the form $P_0 + P_1z + P_2z^2 + z^3$, where the P_n are complicated functions of ℓ , m , \bar{a} , $\bar{\omega}$, and ${}_2A_{\ell m}(\bar{a}\bar{\omega})$ whose exact form is not important to us here. But we do find that $P_{0,1} \rightarrow 0$ as $\bar{a} \rightarrow 0$ allowing for a smooth transition to Eq. (76), and the general form of the physical solution is

$$R(z) = z^{-i\sigma_-}(z-1)^{i\sigma_+}(P_0 + P_1z + P_2z^2 + z^3)e^{i(\bar{r}_+ - \bar{r}_-)\bar{\omega}z}. \quad (83)$$

The TTM_R modes can be found in an analogous manner. We require the physical boundary condition at the event horizon to permit only modes that travel into the black hole. At infinity, we allow only incoming waves. In this case, the condition that the second parameter of the local solution [either Eq. (15) or (16)] must be a nonpositive integer $-q$ has the following forms:

$$-q = \begin{cases} \alpha & (\bar{\zeta}_-, \xi_-, \eta_\pm), \\ \alpha + 1 - \delta & (\bar{\zeta}_-, \xi_+, \eta_\pm), \\ -\alpha + \gamma + \delta & (\zeta_+, \xi_-, \eta_\pm), \\ \alpha + 1 - \gamma & (\bar{\zeta}_-, \xi_-, \eta_\mp). \end{cases} \quad (84)$$

As before, these all reduce to a pair of conditions:

$$q = -1 + s + i \frac{2\bar{\omega}(1 - \sqrt{1 - \bar{a}^2}) - \bar{a}m}{\sqrt{1 - \bar{a}^2}} \quad \text{or} \quad (85a)$$

$$q = -1 + 2s. \quad (85b)$$

Because of the boundary condition at infinity we must consider only positive values for s . For the case of gravitational waves with $s = 2$, we find that the possible solutions given by Eq. (85a) yield no physical solutions, even for $\bar{a} = 0$. The possible solutions given by Eq. (85b) correspond to $q = 3$ and, when $\bar{a} = 0$ yields only one physical solution with $\bar{\omega} = \bar{\Omega}$. The associated solution is

$$\begin{aligned} Hc_{33}(-i\bar{\Omega}, -1, -1 - 4i\bar{\Omega}; z) &= 1 + (\ell - 1)(\ell + 2)z \\ &+ \frac{1}{3}(\ell - 1)^2(\ell + 2)^2z^2 \left(1 + \frac{\ell(\ell + 1)}{3}z \right) \end{aligned} \quad (86)$$

which corresponds to the physical solution

$$\begin{aligned} R(z) &= z^{-2}(z-1)^{-2-2i\bar{\Omega}} \times \\ &\left[1 + (\ell - 1)(\ell + 2)z \right. \\ &\left. + \frac{1}{3}(\ell - 1)^2(\ell + 2)^2z^2 \left(1 + \frac{\ell(\ell + 1)}{3}z \right) \right] e^{-2i\bar{\Omega}z}. \end{aligned} \quad (87)$$

When $\bar{a} \neq 0$, we again find that polynomial solutions are allowed when Eq. (79) is satisfied, except that in this case,

$$\lambda = \lambda_+ \equiv {}_2A_{\ell m}(\bar{a}\bar{\omega}) + \bar{a}^2\bar{\omega}^2 - 2m\bar{a}\bar{\omega} + 4. \quad (88)$$

However, since ${}_{-s}A_{\ell m}(\bar{a}\bar{\omega}) = {}_sA_{\ell m}(\bar{a}\bar{\omega}) + 2s$, we find $\lambda_+ = \lambda_-$ yielding the known result that the TTM_L and TTM_R algebraically special modes share the same frequency spectrum.

The general form of the physical solution is

$$\begin{aligned} R(z) &= z^{-2+i\sigma_-}(z-1)^{-2-i\sigma_+} \times \\ &(1 + P_1z + P_2z^2 + P_3z^3)e^{-i(\bar{r}_+ - \bar{r}_-)\bar{\omega}z}. \end{aligned} \quad (89)$$

In this case, there is no unusual behavior for the P_n coefficients as $\bar{a} \rightarrow 0$. The exact forms of the P_n can be found, but again are not important for this paper.

We can determine the TTMs of Kerr numerically by simultaneously solving the $\Delta_{q+1} = 0$ condition as given by Eq. (79) along with the angular Teukolsky equation, Eq. (4). Equation (79) is an eight-order polynomial in $\bar{\omega}$ whose roots can be found by many methods, and we solve Eq. (4) by the spectral eigenvalue method described in Sec. II D 1. In Fig. 24, we plot the $m \geq 0$ modes for $\ell = 2$ and 3. The modes with $m < 0$ all have $\text{Re}(\bar{\omega}) < 0$ and are the negative frequency counterparts of the $m > 0$ modes as given by Eq. (57). The $m = 0$ cases are especially interesting. The solutions for both $\ell = 2$ and 3 begin, as \bar{a} increases from zero, along the negative imaginary axis. At a critical value of \bar{a} , the solution splits into positive frequency and negative frequency modes again obeying Eq. (57). For $\ell = 2$ the critical rotation rate is $\bar{a} = 0.4944459549$ where $\bar{\omega} = -3.3308102325i$. For $\ell = 3$ it is $\bar{a} = 0.2731627006$ where $\bar{\omega} = -12.182211380i$.

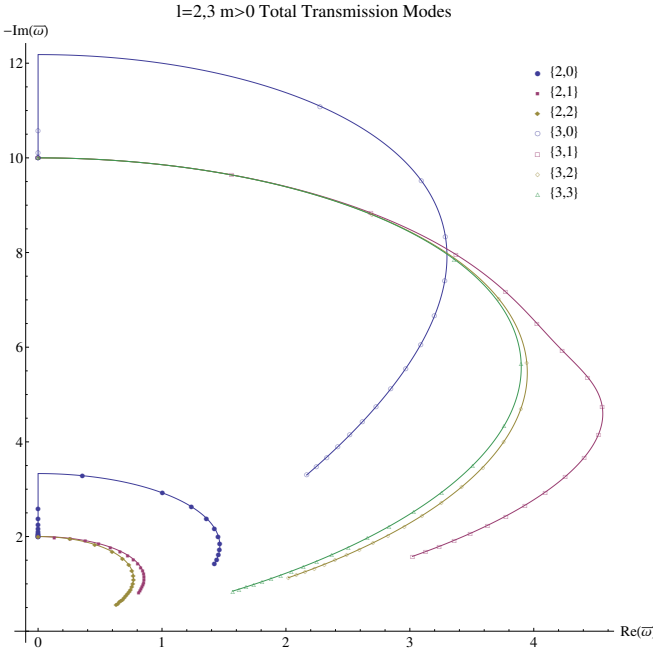


FIG. 24. Kerr algebraically special TTM mode sequences for $\ell = 2$, $m = 0-2$ and for $\ell = 3$, $m = 0-3$. Note that the imaginary axis is inverted and shifted to the left so the $m = 0$ behavior can be more easily seen. Each sequence covers a range $0 \leq \bar{a} \leq 1$, with markers on each sequence denoting a change in \bar{a} of 0.05.

1. Kerr modes in the $\bar{a} = 0$ limit

The existence, or not, of modes (QNM, TTM_L, or TTM_R) at the special frequencies $\bar{\omega} = \bar{\Omega}$ has been the source of considerable confusion (see Refs. [1, 22] for summaries). In summary, it seems that most authors[5, 8, 20, 21] have taken the algebraically special solutions of Kerr to represent the TTMs, with the $s = -2$ solutions representing the TTM_L case and $s = 2$ the TTM_R case, even in the static limit $\bar{a} = 0$ where the frequencies are given by $\bar{\Omega}$. At the same time, numerical solutions[5, 8] seem to suggest that certain QNMs of Kerr approach $\bar{\Omega}$ as $\bar{a} \rightarrow 0$, although numerical difficulties have made it impossible to explore these cases exactly at $\bar{a} = 0$. Onozawa[8] has suggested that the positive- and negative-frequency modes cancel at $\bar{a} = 0$ leading to no QNMs at the special frequencies $\bar{\Omega}$. However, Maassen van den Brink[22] comes to a different conclusion, that there are no TTM_R solutions at $\bar{\Omega}$ and that a certain set of solutions are simultaneously TTM_Ls and QNMs at $\bar{\Omega}$. His arguments are sophisticated, dense, and difficult to follow but ultimately seem to hinge on how one defines an ingoing solution at the event horizon (see Secs. III, VII.A and VII.B of Ref. [22]).

Using the results derived above for the TTM modes, we hope to bring some additional clarity to the confusion. In the Appendix, we present a standard derivation[15] of the asymptotic behavior of solutions at the event horizon

and at infinity. Assuming these definitions remain valid at $\bar{a} = 0$ and $\bar{\omega} = \bar{\Omega}$, then Eq. (77) represents a valid TTM_L solution, and Eq. (87) a valid TTM_R solution, at $\bar{a} = 0$ and $\bar{\omega} = \bar{\Omega}$. The latter is in disagreement with Maassen van den Brink[22].

To examine the behavior of the QNM at the special frequencies $\bar{\Omega}$, we could again look for Heun polynomial solutions but with the $\{\zeta, \xi, \eta\}$ parameters set to prefer QNM solutions. We have done this, but because the characteristic exponents at both the $z = 0$ and $z = 1$ regular singular points differ by an integer we obtain the same TTM_L solution obtained above for $\bar{a} = 0$. However, we can use this TTM_L solution to obtain a second, linearly independent solution of the radial Teukolsky equation at the same frequencies $\bar{\omega} = \bar{\Omega}$. For simplicity, we will use the Heun polynomial of Eq. (82) obtained from the parameter choice $\{\zeta_+, \xi_+, \eta_+\}$. Referring to this solution as $y_1(z)$, we seek a solution $y_2(z) = v(z)y_1(z)$. Using standard methods, we find

$$v'(z) = z^{-3}(z-1)^{1-4i\bar{\Omega}} \left(1 - \frac{\ell(\ell+1)}{3}z\right)^{-2} e^{-4i\bar{\Omega}z}. \quad (90)$$

The corresponding physical solution will have the form

$$R_2(z) = z^2(z-1)^{2i\bar{\Omega}} \left(1 - \frac{\ell(\ell+1)}{3}z\right) e^{2i\bar{\Omega}z} \int v'(z) dz. \quad (91)$$

Expanding about $z = 1$ and integrating, we find

$$v(z) = \frac{f_{(1)}^{(4i\bar{\Omega}-2)}}{(4i\bar{\Omega}-2)!} \ln(z-1) + (z-1)^{2-4i\bar{\Omega}} \sum'_{n=0} \frac{f_{(1)}^{(n)}}{n!(n+2-4i\bar{\Omega})} (z-1)^n, \quad (92)$$

where the prime denotes that the value of $n = 4i\bar{\Omega}-2$ is omitted from the sum, and $f_{(1)}^{(n)} = d^n f(z)/dz^n|_{z=1}$ where $f(z) \equiv (z-1)^{4i\bar{\Omega}-1} v'(z)$. We immediately see that

$$\lim_{z \rightarrow 1} R_2(z) \sim (z-1)^{2-2i\bar{\Omega}}, \quad (93)$$

and this solution obeys the boundary condition at the event horizon for a QNM [see Eq. (A14) or (28b)].

For the boundary at infinity, we find that

$$\lim_{z \rightarrow \infty} v(z) = -e^{-4i\bar{\Omega}z} z^{-4i\bar{\Omega}} \left(\frac{9}{4i\bar{\Omega}\ell^2(\ell+1)^2 z^4} + \mathcal{O}(z^{-5}) \right), \quad (94)$$

giving us

$$\lim_{z \rightarrow \infty} R_2(z) \sim z^{-1-2i\bar{\Omega}} e^{-2i\bar{\Omega}z}. \quad (95)$$

However, this is the behavior of an incoming wave [see Eq. (A13) or (28c)], the incorrect behavior for a QNM. In fact, the two boundary conditions suggest that $R_2(z)$ is a TTM_R (note, however that $s = -2$). What is clear

is that, based on the definitions for incoming and outgoing boundary conditions given in the Appendix, neither Eq. (77) nor (91) are a QNM. Since, for each ℓ , there can be only two linearly independent solutions of the radial Teukolsky equation for $\bar{a} = 0$, $\bar{\omega} = \bar{\Omega}(\ell)$ and $s = -2$, we must conclude that no QNM solutions coincide with the algebraically special solutions of Schwarzschild.

IV. SUMMARY AND DISCUSSION

We have developed an independent code, built as a *Mathematica* package, that can solve the Teukolsky master equation for the QNMs of Kerr. While we use the well-known continued fraction method for solving the radial equation, we have implemented and tested a spectral method for solving the angular equation for the spin-weighted spheroidal function. Using this code, we have performed an extensive, high-accuracy survey of the gravitational QNMs of Kerr. Figures 2–18 display our results for $m \in \{-2, -1, 0, 1, 2\}$, $\ell = 2 \rightarrow 12$, and $n = 0 \rightarrow 7$. These results are quantitatively similar to prior works, improving on prior results only in accuracy.

As a quantitative demonstration of the accuracy and precision of our code, we have carefully explored those QNMs that, in the extreme Kerr limit, approach accumulation points at $\bar{\omega} = m/2$. We have fit these data to extended versions [Eqs. (63) and (64)] of the predicted leading order behavior of $\bar{\omega}$ [Eq. (61)] as $\bar{a} \rightarrow 1$. Equations (63) and (64) also include fitting functions for ${}_{-2}A_{\ell m}(\bar{a}\bar{\omega})$. The high quality of our fitting functions is illustrated in Figs. 19–22 and in Tables I–IV. While our immediate purpose in reporting these details is to help validate our code, Eqs. (63) and (64) and the data in the corresponding tables may be beneficial to anyone trying to find higher-order approximations of the behavior of $\bar{\omega}$ and ${}_{-2}A_{\ell m}(\bar{a}\bar{\omega})$ near the accumulation points.

One of the most interesting topics associated with QNMs is their behavior at the NIA and, in particular, near the algebraically special frequencies $\bar{\Omega}$. We first explored this numerically for the simplest case when $\ell = 2$. For this case, the $n = 8$ overtones approach $\bar{\omega} = -2i$ in the Schwarzschild limit, and the two plots in Fig. 23 show our results. Maassen van den Brink[22] predicted the behavior of the $m \leq 0$ (for positive-frequency) modes and suggested how the corresponding $m > 0$ modes could behave[22, 38]. In contrast to the lower precision solutions considered in Ref. [28], our numerical results for the $m \leq 0$ modes agree very well with Maassen van den Brink's formula, Eq. (65). For small \bar{a} , our results are fit well by Eqs. (67a)–(67c). As previously found in Ref. [28], we also find that the $m > 0$ modes exist as a pair of overtone multiplets. That is, there are $n = 8_0$ overtones for the $m = 1$, and 2 modes that appear to emerge from a single limit frequency given by Eq. (67f), and $n = 8_1$ overtones for the same values of m that appear to emerge from a different limit frequency given by Eq. (67g). In the language of Ref. [38], these limit frequencies could

be unconventional poles on the unphysical sheet beyond the branch cut at the NIA. As \bar{a} increases from zero, the QNMs first appear on the physical sheet at the NIA at some finite value of \bar{a} . Table V displays our numerical values for these modes where they emerge from the NIA. While our results for $m > 0$ are similar to the general behavior described in Ref. [38] neither of our limit frequencies agrees well with their estimates. Furthermore they only find a single limit frequency while the numerical solutions show that there are two.

Throughout this work, we have made use of the theory of confluent Heun functions. It is particularly useful in clarifying how we can ensure that a particular numerical solution will obey some desired pair of boundary conditions. This was, of course, done originally by Leaver[5, 6] for QNMs without explicitly casting the Teukolsky equations as confluent Heun equations, but confluent Heun theory does provide a very useful framework. And perhaps most important, it provides a clear means for finding polynomial solutions. We have given only a few examples of finding these polynomial solutions, but we believe that they may be very useful in understanding the various perturbations of the Kerr space-time.

We rederived the algebraically special TTM_Ls of Kerr as examples of the method for finding confluent Heun polynomial solutions. Without controversy[22], we can say that the polynomial solution of Eq. (83) represents TTM_L modes when $\bar{a} > 0$, and the polynomial solution of Eq. (89) represents TTM_R modes when $\bar{a} > 0$. However, for $\bar{a} = 0$ the situation is not so simple. In the limit that $\bar{a} \rightarrow 0$, Eqs. (83) and (89) smoothly become, respectively, Eqs. (77) and (87). These $\bar{a} = 0$ solutions still satisfy the simple definitions of ingoing and outgoing waves at their boundaries derived in the Appendix, but according to Maassen van den Brink[22] the definitions of ingoing and outgoing waves at the event horizon becomes more complicated in the Schwarzschild limit. He concludes that no TTM_R mode exists for $\bar{a} = 0$ and that Eq. (77) is both a QNM and a TTM_L. These conclusions are rather counterintuitive, and his reasoning is very complicated. As we write this, we do not fully understand all of the subtleties in his arguments, and we are not yet convinced that his conclusions are correct. Our primary concern at this time is that the definitions of ingoing and outgoing solutions at the horizons [see Eqs. (A12) and (A14)] are given in terms of Boyer-Lindquist coordinates. This coordinate system is, itself, singular at the event horizon. As Teukolsky showed[15] by transforming to ingoing Kerr coordinates and performing a spin rotation to obtain a nonsingular null tetrad, the effect of this Boyer-Lindquist singular behavior is a factor of Δ^{-s} in the behavior at the boundary. Terms of this form play an important role in Maassen van den Brink's arguments about the behavior at the boundary and it is not clear to us if he has correctly handled this subtlety.

Appendix A: ASYMPTOTIC BEHAVIOR

In order to explore the behavior of solutions near the horizon r_+ and near infinity, it is useful to rewrite the radial equation in terms of the tortoise coordinate r^* . Following Teukolsky's[15] notation and approach, we define

$$\frac{dr^*}{dr} \equiv \frac{r^2 + a^2}{\Delta}, \quad (\text{A1})$$

$$Y(r^*) \equiv \Delta^{s/2}(r^2 + a^2)^{1/2}R(r), \quad (\text{A2})$$

where we assume $r = r(r^*)$. In the asymptotic limit $r \rightarrow \infty$ ($r^* \rightarrow \infty$), Eq. (5a) becomes

$$\frac{d^2Y(r^*)}{dr^{*2}} + \left(\omega^2 + 2\frac{is\omega}{r}\right)Y(r^*) \approx 0, \quad (\text{A3})$$

which has the two solutions

$$Y(r^*) \sim r^{\pm s}e^{\mp i\omega r^*}. \quad (\text{A4})$$

In terms of the original radial function, and given the sign choice in Eq. (3), we find

$$\lim_{r \rightarrow \infty} R(r) \sim \begin{cases} \frac{e^{-i\omega r^*}}{r^{2s+1}} & : \text{ingoing wave,} \\ \frac{e^{i\omega r^*}}{r^{2s+1}} & : \text{outgoing wave.} \end{cases} \quad (\text{A5})$$

In the asymptotic limit $r \rightarrow r_+$ ($r^* \rightarrow -\infty$), Eq. (5a) becomes

$$\frac{d^2Y(r^*)}{dr^{*2}} + \left(k - is\frac{(r_+ - M)}{2Mr_+}\right)^2 Y(r^*) \approx 0, \quad (\text{A6})$$

where $k \equiv \omega - ma/(2Mr_+)$, which has the two solutions

$$Y(r^*) \sim e^{\pm ikr^*} \left[e^{\frac{(r_+ - M)}{Mr_+}r^*}\right]^{\pm s/2}. \quad (\text{A7})$$

In order to simplify the asymptotic limit, we need to integrate Eq. (A1) for the Tortoise coordinates. The result is

$$r^* = r + \frac{2M}{r_+ - r_-} \left[r_+ \ln\left(\frac{r - r_+}{M}\right) - r_- \ln\left(\frac{r - r_-}{M}\right)\right]. \quad (\text{A8})$$

Now, we let $r = r_+ + \epsilon$ giving us

$$r^*(\epsilon) = r_+ + \epsilon + \frac{2M}{r_+ - r_-} \left[r_+ \ln\left(\frac{\epsilon}{M}\right) - r_- \ln\left(\frac{\epsilon + r_+ - r_-}{M}\right)\right]. \quad (\text{A9})$$

It is then straightforward to show

$$e^{\frac{(r_+ - M)}{Mr_+}r^*(\epsilon)} \propto \Delta + \mathcal{O}(\epsilon^2), \quad (\text{A10})$$

giving us

$$Y(r^*) \sim \Delta^{\pm s/2}e^{\pm ikr^*}. \quad (\text{A11})$$

Then, in terms of the original radial function

$$\lim_{r^* \rightarrow -\infty} R(r^*) \sim \begin{cases} e^{ikr^*} & : \text{ingoing (out of BH),} \\ \Delta^{-s}e^{-ikr^*} & : \text{outgoing (into BH).} \end{cases} \quad (\text{A12})$$

The latter solution, representing waves flowing into the black hole is the physically relevant condition. Note that the unusual term of Δ^{-s} in the physical condition is present because the Boyer-Lindquist coordinates used in Eq. (1) are singular at the horizon. A change of coordinates (cf. Ref. [15]) to a nonsingular coordinate system removes this behavior (but creates a factor of Δ^s in the unphysical condition).

Returning to the standard radial coordinate r via Eq. (A8) gives us the behavior near spatial infinity as

$$\lim_{r \rightarrow \infty} R(r) \sim \begin{cases} r^{-1-2i\omega M}e^{-i\omega r} & : \text{ingoing wave,} \\ r^{-1-2s+2i\omega M}e^{i\omega r} & : \text{outgoing wave,} \end{cases} \quad (\text{A13})$$

where we have used $\lim_{r \rightarrow \infty} e^{i\omega r^*} \propto r^{2i\omega M}e^{i\omega r}$. Near the horizon, $r = r_+$ we find

$$\lim_{r \rightarrow r_+} R(r) \sim \begin{cases} (r - r_+)^{i\sigma_+} & : \text{ingoing (out of BH),} \\ (r - r_+)^{-s-i\sigma_+} & : \text{outgoing (into BH).} \end{cases} \quad (\text{A14})$$

where we have used $\lim_{r \rightarrow r_+} e^{ikr^*} \propto (r - r_+)^{i\sigma_+}$.

- [1] E. Berti, V. Cardoso, and A. O. Starinets, Classical Quantum Gravity **26**, 163001 (2009)
- [2] H.-P. Nollert, Classical Quantum Gravity **16**, R159 (1999)
- [3] S. Chandrasekhar and S. Detweiler, Proc. R. Soc. A **344**, 441 (1975)
- [4] T. Piran and R. F. Stark, in *Dynamical Spacetimes and Numerical Relativity*, edited by J. M. Centrella (Cambridge University Press, Cambridge, England, 1986) pp. 40–73
- [5] E. W. Leaver, Proc. R. Soc. A **402**, 285 (1985)
- [6] E. W. Leaver, J. Math. Phys. (N.Y.) **27**, 1238 (1986)
- [7] H.-P. Nollert, Phys. Rev. D **47**, 5253 (1993)
- [8] H. Onozawa, Phys. Rev. D **55**, 3593 (1997)
- [9] B. Mashhoon, in *Proceedings of the Third Marcel Grossmann Meeting on Recent Developments of General Relativity, Shanghai, 1982*, edited by H. Ning (North-Holland, Amsterdam, 1983)
- [10] V. Ferrari and B. Mashhoon, Phys. Rev. D **30**, 295 (1984)
- [11] B. F. Schutz and C. M. Will, Astrophys. J. Lett. **291**,

- L33 (1985)
- [12] H. Yang, D. A. Nichols, F. Zhang, A. Zimmerman, Z. Zhang, and Y. Chen, Phys. Rev. D **86**, 104006 (2012)
 - [13] S. R. Dolan, Phys. Rev. D **82**, 104003 (2010)
 - [14] S. Hod, Phys. Lett. B **715**, 348 (2012)
 - [15] S. A. Teukolsky, Astrophys. J. **185**, 635 (1973)
 - [16] S. Detweiler, Astrophys. J. **239**, 292 (1980)
 - [17] V. Cardoso, Phys. Rev. D **70**, 127502 (2004)
 - [18] H. Yang, F. Zhang, A. Zimmerman, D. A. Nichols, E. Berti, and Y. Chen, Phys. Rev. D **87**, 041502(R) (2013)
 - [19] H. Yang, A. Zimmerman, A. Zenginoğlu, F. Zhang, E. Berti, and Y. Chen, Phys. Rev. D **88**, 044047 (2013)
 - [20] S. Chandrasekhar, Proc. R. Soc. A **392**, 1 (1984)
 - [21] N. Andersson, Classical Quantum Gravity **11**, L39 (1994)
 - [22] A. Maassen van den Brink, Phys. Rev. D **62**, 064009 (2000)
 - [23] P. P. Fiziev, Classical Quantum Gravity **27**, 135001 (2010)
 - [24] *Heun's Differential Equations*, edited by A. Ronveaux (Oxford University, New York, 1995)
 - [25] R. S. Borissov and P. P. Fiziev, Bulg. J. Phys. **37**, 65 (2010)
 - [26] S. A. Hughes, Phys. Rev. D **61**, 084004 (2000)
 - [27] S. Hod, Phys. Rev. D **78**, 084035 (2008)
 - [28] E. Berti, V. Cardoso, K. D. Kokkotas, and H. Onozawa, Phys. Rev. D **68**, 124018 (2003)
 - [29] P. P. Fiziev, Phys. Rev. D **80**, 124001 (2009)
 - [30] W. Gautschi, SIAM Rev. **9**, 24 (1967)
 - [31] W. H. Press, S. A. Teukolsky, W. T. Wetterling, and B. P. Flannery, *Numerical Recipes in C*, 2nd ed. (Cambridge University Press, Cambridge, England, 1992)
 - [32] M. Sasaki and T. Nakamura, Prog. Theor. Phys. **67**, 1788 (1982)
 - [33] E. D. Fackerell and R. G. Crossman, J. Math. Phys. (N.Y.) **18**, 1849 (1977)
 - [34] M. A. Blanco, M. Flórez, and M. Bermejo, J. of Mol. Struct.: THEOCHEM **419**, 19 (1997)
 - [35] K. Glampedakis and N. Andersson, Phys. Rev. D **64**, 104021 (2001)
 - [36] W. E. Couch and E. T. Newman, J. Math. Phys. (N.Y.) **14**, 285 (1973)
 - [37] R. M. Wald, J. Math. Phys. (N.Y.) **14**, 1453 (1973)
 - [38] P. T. Leung, A. Maassen van den Brink, K. W. Mak, and K. Young, Classical Quantum Gravity **20**, L217 (2003)